Confidential manuscript submitted to Journal of Geophysical Research-Atmospheres

A CloudSat and CALIPSO-based evaluation of the effects of thermodynamic instability and aerosol loading on Amazon Basin deep convection and lightning

Dale Allen[1], Kenneth Pickering[1], Melody Avery[2], Zhanqing Li[1,3], Siyu Shan[1], Carlos Augusto Morales Rodriguez[4], and Paulo Artaxo[5]
[1]Department of Atmospheric and Oceanic Science, University of Maryland
[2]NASA Langley Research Center
[3]Earth System Science Interdisciplinary Center (ESSIC) University of Maryland
[4]Instituto de Astronomia, Geofisica, e Ciénces Atmosféricas, Universidade de Sao Paulo
[5]Instituto de Fisica, Universidade de Sao Paulo

Corresponding author: Dale Allen (djallen@umd.edu)

Submitted

J. Geophysical Research-Atmospheres

Key Points:

After controlling for CAPE, thunderstorms developing in dirty environments are 1.5 km deeper than storms developing in clean environments.

After controlling for CAPE, upper tropospheric ice water content is 50% greater for storms developing in dirty conditions versus clean conditions.

After controlling for CAPE, flash rates are a factor of 2 or more greater for storms developing in dirty conditions versus clean conditions.

Abstract

The Amazon Basin, which plays a critical role in the carbon and water cycle, is under stress due to changes in climate, agricultural practices, and deforestation. The effects of thermodynamic and microphysical forcing on the strength of thunderstorms in the Basin (75-45° W, 0-15° S) were examined during the pre-monsoon season (mid-August through mid-December), a period with large variations in aerosols, intense convective storms, and plentiful flashes. The analysis used measurements of radar reflectivity, ice water content (IWC), and aerosol type from instruments aboard the CloudSat and CALIPSO satellites, flash rates from the ground-based STARNET network, and total aerosol optical depth (AOD) from a surface network and a meteorological re-analysis. After controlling for convective available potential energy (CAPE), it was found that thunderstorms that developed under dirty (high-AOD) conditions were 1.5 km deeper, had 50% more IWC, and more than two times as many flashes as storms that developed under clean conditions. The sensitivity of flashes to AOD was largest for low values of CAPE where increases of more than a factor of three were observed. The additional ice water indicated that these deeper systems had higher vertical velocities and more condensation nuclei capable of sustaining higher concentrations of water and large hydrometeors in the upper troposphere. Flash rates were also found to be larger during periods when smoke rather than dust was common in the lower troposphere, likely because smoky periods were less stable due to higher values of CAPE and AOD and lower values of mid-tropospheric relative humidity.

Plain Language Summary

The Amazon Basin, which plays an important role in the carbon and water cycle, is under stress due to changes in climate, agricultural practices, and deforestation. The Basin includes a rainforest in the northwest and a mix of deforested areas, savannah-type vegetation, and agriculture in the southeast. The effects of instability and aerosol loading on thunderstorms in the Basin (75-45° W, 0-15° S) were examined during mid-August through mid-December, a period with large variations in aerosols, intense convective storms, and plentiful flashes. The analysis used measurements of radar reflectivity, ice water content (IWC), and aerosol type from instruments aboard the CloudSat and CALIPSO satellites, flash rates from the ground-based STARNET network, and aerosol optical depth (AOD) from a surface network and a meteorological re-analysis. After controlling for convective available potential energy (CAPE), a measure of instability, it was found that thunderstorms that developed under dirty (high-AOD) conditions were approximately 1.5 km deeper, had 50% more IWC, and more than two times as many flashes as storms that developed under clean (low-AOD) conditions. Flash rates were also found to be larger during periods when smoke rather than dust was common in the lower troposphere, likely because these periods were less stable.

1 Introduction

Deep convection requires low-level convergence, boundary layer moisture, and instability. Tao et al. (2012), Li et al. (2017), and Fan and Li (2022) review the intimate connection between aerosols and deep convection. Many aerosol particles are hygroscopic and serve as efficient cloud condensation nuclei (CCN) when activated. Activated cloud droplets grow by both condensation and coalescence, with the much faster coalescence process becoming increasingly important as cloud droplets rise through the cloud and grow (Freud et al., 2011; Freud and Rosenfeld, 2012; McFiggans et al., 2006). The height cloud droplets must reach before coalescence dominates over condensation increases with aerosol optical depth (AOD) (Zhu et al., 2015). Therefore, the onset of coalescence in convection occurring at polluted locations may be delayed until droplets rise to altitudes where temperatures are sub-freezing, and glaciation is possible (Rosenfeld et al., 2008). Thus, adding aerosols may create more but smaller liquid droplets that rise to higher altitudes leading to a suppression of warm rain and an invigoration of deep convection and lightning (Khain et al., 2005; Koren et al., 2005; 2010; Y. Liu et al., 2020; Lohmann, 2008; Niu and Li, 2012; Petersen and Rutledge, 2001; Yang and Li, 2014). Within a convective mixed-phase layer, interactions between graupel and ice crystals in the presence of supercooled water lead to efficient charge transfer, electric field growth, and lightning (Blyth et al., 2001; Saunders et al., 2006; Takahashi, 1978).

Observations and numerical simulations suggest that adding aerosols to a pristine environment intensifies deep convection through aerosol-induced changes in the mixed phase layer of the cloud that enhance lightning (Fan et al., 2018). As the aerosol amount continues to increase, a larger population of tiny droplets begins to suppress the growth of graupel and the delivery of large, supercooled droplets to the mixed phase region thus suppressing charge separation and flash rates (Williams et al., 2002). For larger aerosol amounts, the aerosol invigoration effect is opposed by an aerosol radiative forcing effect that stabilizes the atmosphere and lessens the intensity of deep convection (Andreae et al., 2004; Koren et al., 2008; Manoj et al., 2021; Rosenfeld, 1999; Wang et al., 2013; Williams et al., 2002; Yang et al., 2013; Yuan et al., 2011). The combined impact of the opposing effects under polluted conditions may delay the development of intense storms until later in the day (Guo et al., 2016; Lee et al., 2016) and can lead to increases or decreases in rainfall depending on atmospheric humidity, buoyancy, and windshear (Khain, 2009). Albrecht et al. (2011) found that aerosols enhanced lightning activity in the Amazon basin, but the effect was statistically significant only during the wet season. Fan et al. (2009, 2016) found that microphysical invigoration is largest in moist environments with minimal wind shear, warm cloud bases, and ample convective available potential energy (CAPE) such as the tropical western Pacific and southeastern China. Storer et al. (2014) examined the sensitivity of four CloudSat deep convective parameters to AOD over the eastern North Atlantic using CloudSat data for 2006-2009 and aerosol fields from an aerosol assimilation system (Hollingsworth et al., 2008). After controlling for CAPE and lower tropospheric static stability (LTSS), they found that increases in the radar reflectivity centroid (Z_{re}) (Heiblum et al., 2012; Koren et al., 2009), cloud top height, rain top height (highest layer for which radar reflectivity (Z_e) >0), and ice water path (IWP) with AOD were statistically significant both in deep convective cores and in the surrounding stratiform region. Buiat et al. (2017) examined the characteristics of clouds conducive to lightning formation using CloudSat products and lightning data from twelve convective events over Italy. They found a strong correlation between the number of strokes and the vertical distribution of ice particles, with lightning discharges most common when ice water content (IWC) and effective radius values were large at mid-and-upper levels (Takahashi, 1978). Peng et al. (2015) examined the sensitivity of deep convective cloud heights to aerosol loading using aerosol amounts from Moderate Resolution Imaging Spectrometer (MODIS) and cloud top heights from CloudSat. They found that tropical cloud top heights over land increased by 2-4 km as AOD increased from 0.1 to 0.5, with larger increases for mixed-phased clouds with warm bases (T > -15° C) than for mixed-phase clouds with cold bases. An aerosol invigoration signal was not found in several other studies. For example, Veals et al. (2022) examined the impact of aerosols on the depth of deep convective storms using measurements from the Cloud, Aerosol, and Complex Terrain Interactions (CACTI) campaign that took place from October 2018 to April 2019 in central Argentina. They found that the 15 dBZ echo top height increased strongly with the level of neutral buoyancy (LNB) and with CAPE. Echo top heights also increased with AOD; however, after accounting for correlations with meteorological variables, increasing AOD was generally correlated with higher cloud top temperatures and a decrease in the vertical extent and intensity of deep convection. Grabowski and Morrison (2020) used a model to examine convective development over Amazonia. They found that adding additional ultrafine CCN led to increased cloud buoyancy, stronger updrafts, and thus more condensation below the freezing level; however, they did not observe what is traditionally called convective invigoration, i.e., an impact at altitudes above the freezing level.

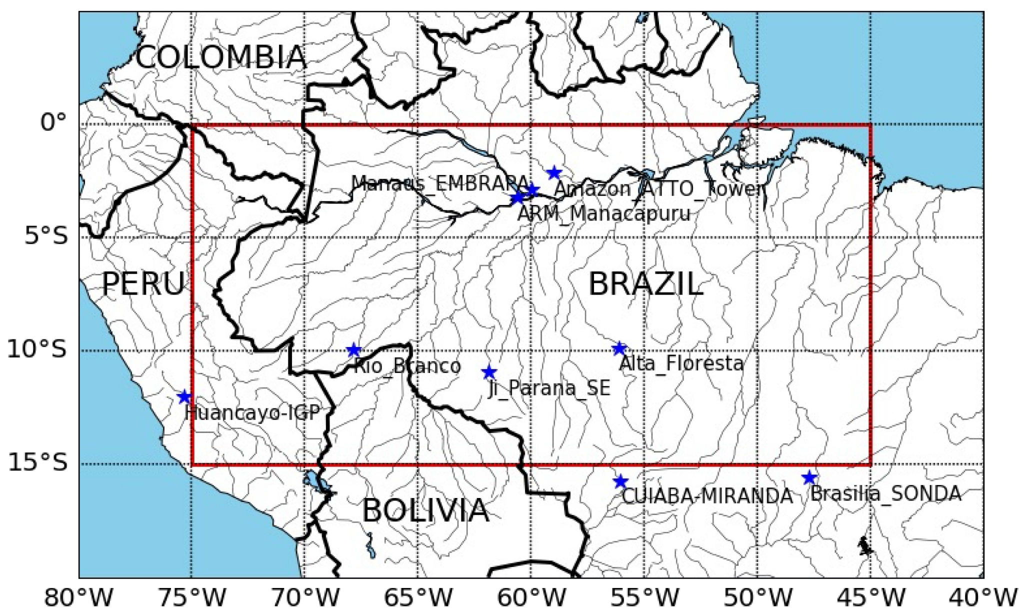

Figure 1. Map showing region of interest. The Amazon Basin (75° - 45° W, 15 - 0° S) is highlighted with a black rectangle. The locations of the nine AERONET sites used in this study are shown with blue stars.

In this study, the relationship between aerosols, deep convection, precipitation, and lightning is examined over the Amazon Basin (75-45° W, 0-15° S) (see Figure 1) using CAPE from the ERA5 reanalysis, total column optical depth from AERONET (Palacios et al., 2022) and the

MERRA-2 reanalysis (Buchard et al., 2017), precipitation rates from IMERG (Huffman et al., 2019, 2020), flash rates from the Sferics Timing and Ranging Network (STARNET) (Morales-Rodriguez et al., 2011), estimates of convective intensity and aerosol type derived from CloudSat (Stephens et al., 2002) and CALIPSO (Winker et al., 2009; 2010), and profiles of relative humidity (RH) and temperature obtained from ancillary European Centre for Medium-Range Weather Forecasts (ECMWF) products (Cronk and Partain, 2017).

The Amazon Basin is an area that includes the Amazon rainforest in the northwest and a mix of deforested areas, savannah-type vegetation, and agriculture in the southeast (Kumar et al., 2023; Ter Steege et al., 2013). Climate change and deforestation are affecting the air quality and weather, increasing the Basin's susceptibility to drought, especially in the southeastern portion of the Basin (Wunderling et al., 2022). Biomass burning associated with agricultural practices and deforestation enhances the concentration of aerosols (Mataveli et al., 2021), especially during the dry season when mean concentrations of particles are ten times greater than during the wet season (Artaxo et al., 2002, 2022). Changes in the thermodynamic environment associated with this drying are also impacting the abundance of smoke and dust in the atmosphere, the amount of rainfall (Saad et al., 2010), and the frequency and intensity of deep convection and lightning (Albrecht et al., 2011; Altaratz et al., 2010; Morales-Rodriguez, 2019). Therefore, this region is an ideal location to study the evolving relationship between thermodynamics, microphysics, aerosol amounts, precipitation rates, and ultimately flash rates.

Albrecht et al. (2011) examined variations in convective intensity during the mid-September to mid-November transition between dry and wet seasons over Rondonia. They found that storms were more intense (i.e., had higher percentages of positive cloud-to-ground (+CG) flashes, and higher 30 dBZ echo top heights) during the dry season (mid-September to early October at this location) than the transition or wet seasons. They also found that the intensity of storms was independent of aerosol concentrations early in the period when aerosol concentrations were high but increased with aerosol concentrations beginning October 20th, when the lower concentrations allowed an aerosol-limited regime to be established. Wall et al. (2014) studied the impact of aerosols on convective features over the Amazon, central Africa, the tropical Atlantic, and the North American Monsoon (NAM) regions using 10 years of TRMM Precipitation Radar data on convective storms and 5 years of CloudSat data on cumulus congestus clouds. In the Amazon Basin, they found that convective storms forming in more polluted conditions based on MODIS aerosol index (AI) values had 30% more rain, 4.5 × more lightning, 2 km higher cloud tops as determined using the metric maximum height of 20 dBZ echo, and more ice scattering (85-GHz polarization-corrected temperatures were 9 K lower) than storms forming over clean regions. Stolz et al. (2015) examined the impact of thermodynamics and aerosols on the intensity of deep convection and flash rates using data on convective features observed by TRMM. They found that the lightning density decreased with warm cloud depth (WCD), i.e., the vertical thickness between the lifting condensation level (LCL) and the freezing level. When WCD was held constant, total lightning density (TLD) over continents increased by approximately 170% between low and high values of aerosols with diameters greater than 40 nm (N40). Altaratz et al. (2017) studied the link between aerosol loading and convective activity over several regions including the Amazon. Over the Amazon, they found that Worldwide Lightning Location Network (WWLLN) flash densities (Virts et al., 2013) in polluted air exceeded those in clean air by approximately a factor of two during March-May, 2012 for CAPE values between 500 and

2500 J kg^{-1}. Jiang et al. (2018) examined the impact of aerosol type on the intensity of deep convection over three regions of the globe including South America (0° –30° S, 35° −80° W). Over South America, they found that values of the IWC centroid (Z_{IWC}) were lower when the CALIOP aerosol type Elevated Smoke was dominant and higher when Polluted Continental Smoke (PCS) was dominant. The response of Z_{IWC} to aerosol perturbations was found to be non-monotonic consistent with several studies that show a turning point in the response of convective metrics and flashes to AOD due to the competing influences of microphysical and radiative effects (Wang et al., 2018).

This study expands on these previous studies that examine the combined impact of thermodynamics and aerosols on the intensity of deep convection in the Amazon Basin. Section 2 describes the data products and methodology, section 3 examines the sensitivity of convective intensity to observed and reanalysis-based estimates of total column AOD after controlling for CAPE, and section 4 offers conclusions.

2 Methodology and Data Products

This study focuses on the pre-monsoon period defined here to be August 16 to December 15. This period is focused on because it has large variations in aerosols, continental conditions, and high lightning activity (Petersen and Rutledge, 2001; Saraiva et al., 2016). It is a period when the CAPE threshold for deep convective storms is low, and the percent of clouds that are cumulonimbus is the largest (Wu and Lee, 2019). In addition, more thunderstorms form during this period because it is a transition period that occurs after aerosol sources have built up over the dry season but before the most intense rainfall (monsoon). The onset of the rainy season in the Amazon Basin varies with location and year but can begin as late as mid-December (Marengo et al., 2001). The range of years examined is 2012 – 2017. This time period was chosen because it is a period with flash data from STARNET that encompasses CloudSat Epoch 6 that began on May 15, 2012 when CloudSat returned to the A-Train formation enabling overlap with ancillary data from MODIS and CALIPSO and ended in early 2018 when CloudSat exited the A-train. In this study, CloudSat data are available for May 15, 2012 through December 5, 2017, while CALIPSO data used in estimating the aerosol type are available for most days during the 2012-2017 time period.

2.1 CloudSat Products

CloudSat is a satellite launched in April 2006 that carries a radar capable of penetrating cloud tops and examining the internal structure and microphysics of deep convective clouds (Stephens et al., 2002). CloudSat with an equator crossing time of 1:30 PM during the period of this study contains a W-band (94-GHz) nadir-looking Cloud Profiling Radar (CPR) with a 1.1 km footprint and a 480 m vertical resolution that can be used to observe relatively small cloud hydrometeors (Tanelli et al., 2008). The primary CloudSat variables used in this study are profiles of cloud type from the 2B-CLDCLASS data set (Sassen and Wang, 2008), profiles of radar reflectivity (Z_e) obtained from the 2B-GEOPROF data set (Mace and Zhang, 2014; Marchand et al., 2008; Protat et al., 2009) and profiles of ice water content (IWC) (Deng et al., 2013, 2015) obtained from the 2C_ICE product. The product version used in this study is Revision 05. The 2C-ICE product uses Z_e along with attenuated backscattering coefficients at 532 nm ($\boldsymbol{\gamma}$') from the

CALIPSO lidar (see section 2.2) to constrain the ice cloud retrieval more tightly than a radar-only product that is also available but not used in this study. The microphysically-constrained ice water path (IWP-MP) (g m^{-2}) is also read in from the 2C_ICE data sets and used in the analysis. The centroid or center-of-gravity of IWC (Z_{IWC}) is calculated by weighting the altitude of the CloudSat layers (Z) by the IWC (Jiang et al., 2018). Mathematically,

$$Z_{IWC} = \sum_{k_1}^{k_2} IWC(k) \cdot Z(k) \Big/ \sum_{k_1}^{k_2} IWC(k)$$

where the summations start at the above-ground CloudSat layer with the highest value of Z_e (K1) and end with the highest CloudSat cloud layer (K2). Similarly, the centroid of radar reflectivity (called Z_{re} here but the center of gravity by Storer et al., 2014) is calculated by weighting Z by the radar reflectivity (Z_e). Mathematically,

$$Z_{re} = \sum_{k_1}^{k_2} Z_e(k) \cdot Z(k) \Big/ \sum_{k_1}^{k_2} Z_e(k)$$

where the summation starts at the above-ground CloudSat layer with the highest value of Z_e (K1), ends with the highest CloudSat cloud layer (K2), and only includes layers for which Z_e is greater than zero.

The metrics Z_{IWC} and Z_{re} are used to assess the intensity of deep convective systems sampled by CloudSat and CALIPSO. In order to compare the intensity of systems, representative values of Z_{IWC} and Z_{re} were determined for each deep convective system observed by CloudSat during the 2012-2017 time period. The CloudSat algorithm determines the cloud type using information that includes the maximum Z_e measured by the CPR, the presence of precipitation, the temperature profile, and the height of surface topography (Marchand et al., 2008; Sassen and Wang, 2008). Only profiles with clouds typed as deep convective are used in this study. Deep convective clouds were present in 3% of CloudSat profiles over Amazonia (Dodson et al., 2018). A deep convective system is defined here to consist of five or more adjacent CloudSat profiles that contain at least one layer that is typed as deep convective by CloudSat. However, the adjacency requirement is waived if two groups of deep convective retrievals are separated by just one retrieval that does not contain a deep convective layer. In that instance, the two groups are combined into one system. The location of each system is obtained by averaging the latitude and longitudes of individual profiles within the system. Similarly, representative values of convective metrics, including Z_{IWC} and $Z_{re,}$ are obtained for each system by averaging values from the individual retrievals. Means are used instead of maxima because maxima are sensitive to the number of profiles in a system, which varies significantly between convective systems.

2.2 CALIPSO Products

In addition to the CloudSat radar, the companion satellite CALIPSO (Winker et al., 2009; 2010) contains a lidar (Hunt et al., 2009) for use in examining the properties of clouds and aerosols in detail. In this study, information from CALIPSO is incorporated into the estimate of IWC and IWP (see section 2.1) and is critical in estimating the type of aerosol present when deep convective systems develop. In this study, we used both daytime and nighttime v4.2 Lidar Level 2 CALIPSO aerosol types (Kim et al., 2018). Important CALIPSO variables used in estimating the aerosol type are the Level 1 estimated particulate depolarization ratio ($\boldsymbol{\delta}_p$) and the Level 1 532 nm integrated attenuated backscatter ($\boldsymbol{\gamma}$') (Kim et al., 2018). $\boldsymbol{\gamma}$'is useful for determining how much aerosol is present in an aerosol layer, while $\boldsymbol{\delta}_p$ is useful for determining the sphericity of aerosol particles. The depolarization ratio increases with the fraction of non-spherical particles in an aerosol layer. Over land, CALIOP layers with $\boldsymbol{\delta}_p > 0.20$ are assumed to be Dust, while layers with $0.075 < \boldsymbol{\delta}_p < 0.20$ are assumed to be Polluted Dust. Layers over land with $\boldsymbol{\delta}_p < 0.075$ and $\boldsymbol{\gamma}' < 0.0005$ are assumed to be Clean Continental, while layers with $\boldsymbol{\delta}_p < 0.075$ and $\boldsymbol{\gamma}' > 0.0005$ are assumed to be Elevated Smoke if the top of the aerosol layer (Z_{top}) is located above 2.5 km and Polluted Continental Smoke (PCS) for $Z_{top} < 2.5$ km. A small percentage of grid boxes in the northeastern portion of the study region are located over water. See Kim et al. for more details on how aerosol typing is done for these retrievals. While considerable effort has gone into evaluating and refining CALIOP aerosol types (e.g., Mielonen et al., 2009; Papagiannopoulos et al., 2016), the information available to discriminate aerosol types is limited. For example, the only difference between Polluted Continental Smoke and Elevated Smoke is the altitude of the aerosol layer, while the only difference between Dust and Polluted Dust is the value of $\boldsymbol{\delta}_p$.

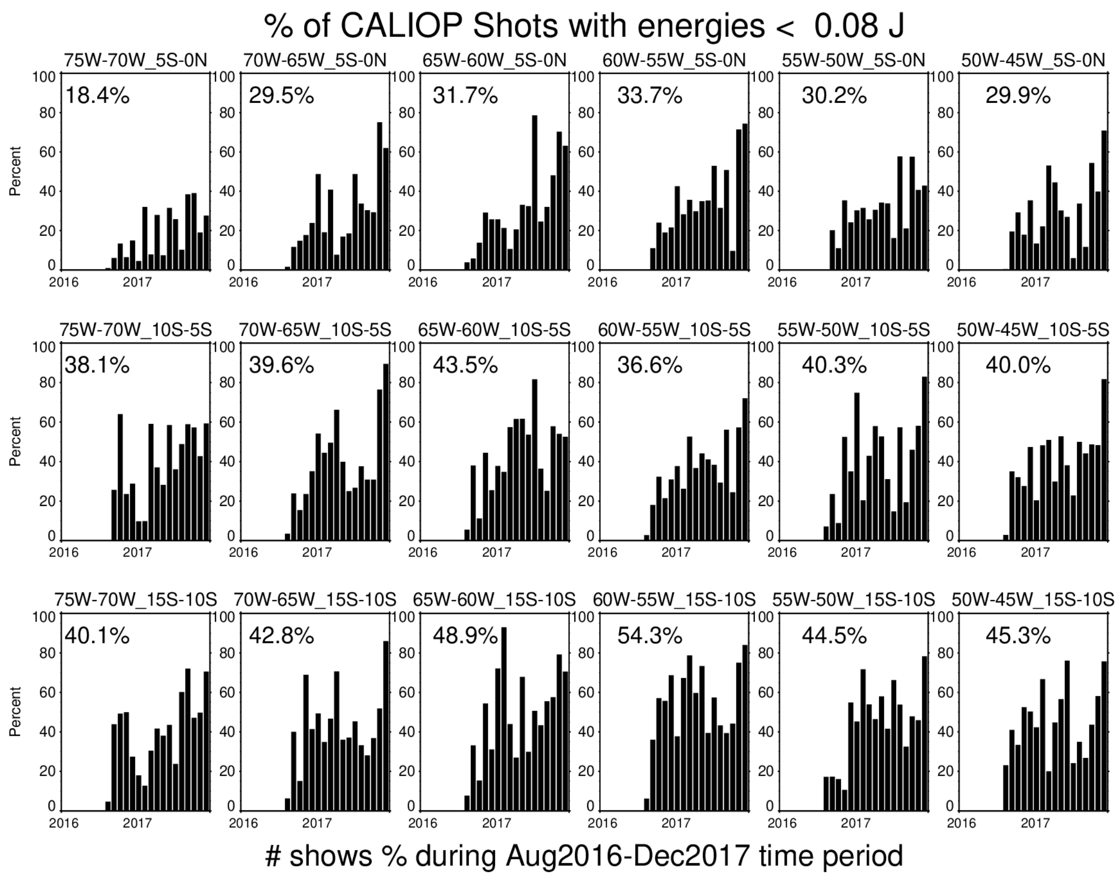

Figure 2. Time series showing percent of CALIOP shots that are low-energy as a function of month over the 2016-2017 time period. Values are shown for eighteen 5° × 5° grid boxes within the Amazon Basin. The percents shown in the upper left of each plot are means over the August 2016 – December 2017 time period.

Since mid-2016, an increasing percentage of the pulses emitted by the CALIPSO lidar have been low energy due to pressure losses in the canister housing the laser (Tackett et al., 2022). Low energy CALIPSO retrievals, i.e., retrievals with energies of less than 0.08 J, occur most frequently in the South Atlantic Anomaly, a high radiation region that includes the southern portion of the Amazon Basin. Low-energy shots were rare in the Amazon Basin until August 2016. Figure 2 shows the time series of the low-energy shot frequency for 5° × 5° regions in the Amazon Basin over the 2016-2017 time period. For the August 2016 to December 2017 period, the percentage of low-energy shots ranged from 20-30% in the northern portion of the Basin to 40-55% in the southern portion of the domain. By late 2017, the percentage of low-frequency shots was 30-50% in the northern Basin and 50-80% in the southern Basin. Low-energy CALIOP retrievals are of lower quality and are not used in this study as recommended by the CALIPSO team. A minor consequence of the increase in low-energy shots is that the aerosol typing used in this study is biased towards 2012-2015 when more data are available.

When possible, the dominant aerosol type is identified for each deep convective system using only high-energy (> 0.08 J), high-confidence extinction retrievals. As suggested by the CALIPSO team (Z. Liu et al., 2018; Tackett et al., 2018; Vaughan et al., 2009), we filtered the aerosol profiles to include extinction quality flags of 0 or 1, indicating semi-transparent aerosol layers and 16 or 18 indicating opaque aerosol layers (see section 5.3.1 of Tackett et al., 2018). We included layers with Cloud-Aerosol-Discrimination (CAD) scores between -100 and -20 inclusive. CAD scores range from -100 to 100, with -100 indicating complete confidence that a feature is an aerosol and a value of 100 indicating complete confidence that a feature is a cloud. When possible, the CALIOP data set contains an estimate of the aerosol type for each layer. In order to estimate the dominant aerosol type associated with each convective system, we extracted all nighttime and daytime CALIOP retrievals within the 1° × 1° grid box containing the system on the day of the system. We then examined the aerosol type for all layers with pressures greater than 675 hPa. The pressure threshold is set to 675 hPa, ~ 3 km for a convective boundary layer because the air from higher layers of the atmosphere is less likely to be ingested into a storm and affect its development. The most common aerosol type was then assumed to be representative of the grid box and convective system. One of the caveats of this simplistic approach for determining the aerosol type associated with each system is that it does not consider the amount of aerosol in each layer, intra-day variations in aerosol type, the impact of multiple aerosol layers of different types, or give weight to variations in the horizontal resolution (5, 20, or 80 km) of the retrieved layers.

Using the v4.2 CALIPSO AOD retrieved for each aerosol layer, we determined aerosol loading by dust and smoke. By summing the AOD values for lower tropospheric layers typed as Polluted Dust, Dust, and Dusty Marine, an estimate of the AOD due to dust was obtained for each profile (AOD_Dust). By summing the AOD values for layers typed as Elevated Smoke and PCS, each profile obtained an estimate of the AOD due to smoke (AOD_Smoke). The sums from all profiles on a given day were averaged to obtain an estimate of the AOD due to smoke and dust on that day. The time series of two-week mean AOD_Dust and AOD_Smoke for the 2012-2017 time period are shown later in this manuscript (see Figure 3 described in section 3.1).

2.3 Thermodynamic metrics

CAPE, an indicator of the instability of the atmosphere, was used to identify large-scale environments favorable for the development of intense storms with lightning (N. Liu et al., 2020). CAPE is often used in conjunction with other variables, such as updraft velocity (Choi et al., 2005) or precipitation (Romps et al., 2014), to estimate flash rates. Gridded hourly values of CAPE are available at 0.25° × 0.25° resolution from the ERA5 reanalysis (Hersbach et al., 2020) that was produced by blending ECMWF forecasts with observations using four-dimensional variational data assimilation. For each deep convective system, CAPE was extracted in the 1° × 1° grid box containing the system for the three-hour period ending at the time of the CloudSat overpass. The maximum of the three-hourly values was taken, assumed to be representative of the thermodynamic environment, and will be used in this analysis.

The intensity of deep convective storms also varies with lower tropospheric static stability and mid-tropospheric relative humidity (RH) (Wall et al., 2014), which is defined here as the mean RH of deep convective cloud layers between 3 and 7 km above mean sea level (MSL). Temperature and RH profiles corresponding to the CloudSat cloud profiling bins were read from version P1_R05 of the ECMWF-AUX data set (Cronk and Partain, 2017).

2.4 Metrics of aerosol loading

Information on the total column aerosol amount over Amazonia was obtained from the Aerosol Robotic Network (AERONET) (Andreae et al., 2015; Esteven et al., 2019; Holben et al., 2001; Palacios et al., 2022) and version 2 of the Modern-Era Retrospective analysis for Research and Applications (MERRA-2) (Gelaro et al., 2017).

AERONET is a ground-based remote sensing aerosol network that provides column aerosol optical depth (AOD) data at numerous global locations. The network has 9 locations with extensive Amazon Basin data during the 2012-2017 time period (Table 1). This study uses version 3 AERONET AOD values with Spectral Deconvolution Algorithm (SDA) Retrieval Level 2. These values are cloud-cleared and quality assured with pre-field and post-field calibrations applied. The seasonality of aerosol optical properties over the Amazon is discussed in Schafer et al. (2008). They find low concentrations of aerosols throughout the Basin during the first half of the year with dramatic increases, especially in the southern forested region and the adjacent cerrado (woodland/savanna) region to its east, with the onset of the burning season in September.

The MERRA-2 system includes the Goddard Chemistry, Aerosol, Radiation and Transport (GOCART) model (Chin et al., 2002) integrated into version 5 of the Goddard Earth Observing System Model (GEOS-5) and an assimilation system that assimilates meteorological parameters as well as aerosols (Buchard et al., 2017). Aerosol products that are assimilated include aerosol optical depth (AOD) from Advanced Very High-Resolution Radiometer (AVHRR), MODIS (Remer et al., 2008), Multi-angle Imaging Spectro-Radiometer (MISR) (Kahn et al., 2005) over bright surfaces, and AERONET (Randles et al., 2017). The distribution of organic carbon, black carbon, sea salt, dust, and sulfate aerosols is output by the MERRA-2 system. Hourly 0.625° × 0.5° horizontal resolution MERRA-2 AOD was used in this study (GMAO, 2015). For each deep convective system, the MERRA-2 AOD was extracted at the location of the centroid of the system in the hour containing the CloudSat/CALIPSO overpass and is assumed to be representative of the system. It is important to note that the MERRA-2 AOD is a total column, which includes the stratosphere. Thus, the MERRA-2 column could be impacted by stratospheric aerosols that are unlikely to be ingested into a convective storm.

Table 1. AERONET sites used in this analysis.

Location	Longitude	Latitude	First Day with Observations	Last Date with Observations	Days[a]	Obs[b]
Huancayo-IGP	75.32° W	12.04° S	Mar 20, 2015	Dec 30, 2017	298	11990
Rio Branco	67.87° W	9.96° S	Jan 16, 2012	Oct 30, 2017	347	3875
Ji Parana SE	61.85° W	10.93° S	Jan 1, 2012	Dec 29, 2017	379	4073
Manaus EMBRAPA	59.97° W	2.89° S	Jan 1, 2012	Dec 28, 2017	337	3049
ARM Manacapuru	60.60° W	3.21° S	Dec 20, 2013	Nov 30, 2015	83	835
Amazon ATTO Tower	59.00° W	2.14° S	Mar 10, 2016	Dec 29, 2017	149	1116
Greater Manaus[c]	59.86° W	2.78° S	Jan 1, 2012	Dec 29, 2017	429	5000
Alta Floresta	56.10° W	9.87° S	Jan 28, 2012	Dec 31, 2017	406	3915
Cuiaba-Miranda	56.07° W	15.73° S	Jan 3, 2012	Dec 30, 2017	394	4158
Brasilia-SONDA	47.71° W	15.60° S	Sep 16, 2015	Dec 7, 2016	107	1119

[a]Days refers to the number of days during 2012-2017 with observations during the pre-monsoon period
[b] Obs refers to the number of observations during the pre-monsoon period
[c] *Greater Manaus* is a fictional site created using measurements from the Manaus EMBRAPA site, the ARM Manacapuru site that was active during the GoAmazon experiment (Martin et al., 2017), and the Amazon Tall Tower Observatory (ATTO) that has been active since March 2016 (Andreae et al., 2015). The ATTO tower is upwind of the city of Manaus (>1 million population). EMBRAPA is in/near the city, and the ARM site was downwind of the city.

2.5 Precipitation and Lightning Products

Precipitation data were taken from the Integrated Multi-satellitE Retrievals for Global Precipitation Mission (IMERG) (Huffman et al., 2019, 2020). The IMERG algorithm merges intercalibrated estimates of precipitation from passive microwave and infrared sensors aboard the Tropical Rainfall Measuring Mission (TRMM, 2000-2014) and Global Precipitation Mission (GPM, 2014-present) satellites, precipitation gauges, and other sources to estimate the rain rate at a 30-minute temporal and 0.1° × 0.1° horizontal resolution. In this application, we use the gridded L3 research quality final product, which has been calibrated using monthly rain gauge data. For use with other products, the 0.1° × 0.1° 30-minute resolution IMERG precipitation was aggregated onto a 1° × 1° grid over the 2012-2017 time period

Lightning flashes were provided by the South American VLF long-range lightning detection network known as Sferics Timing and Ranging Network (STARNET) (Morales-Rodriguez et al., 2014). STARNET is a ground-based network composed of 13 VLF sensors distributed over South America (9 sensors), North America (1), the Caribbean (1), and Africa (2) that measure sferics (radio noise emitted by lightning discharges). To determine the lightning location, STARNET uses the arrival time difference (ATD) method that requires at least four sensors (Morales-Rodriguez et al., 2014). This lightning network detects mostly cloud-to-ground strokes of both polarities that are clustered into flashes using a time and space constraint proposed by Cummins et al. (1998), i.e., 1 second and 15-km. STARNET has a stroke detection efficiency of 35% (~70% for flashes) and a location error varying from 2 to 5 km over South America (Morales-Rodriguez et al., 2014). In this analysis, there is no adjustment for detection efficiency, and all flashes are included regardless of the value of the quality control flag. For most applications, flashes for the 2012-2017 time period are read in for each day and gridded at a 10-minute temporal and a 0.1° × 0.1° horizontal resolution. For comparison with IMERG precipitation and other variables, STARNET flashes were accumulated over 30-minute periods and aggregated onto the same 1° × 1° grid.

3 Results

3.1 Climatological variations in variables of interest over the Amazon Basin

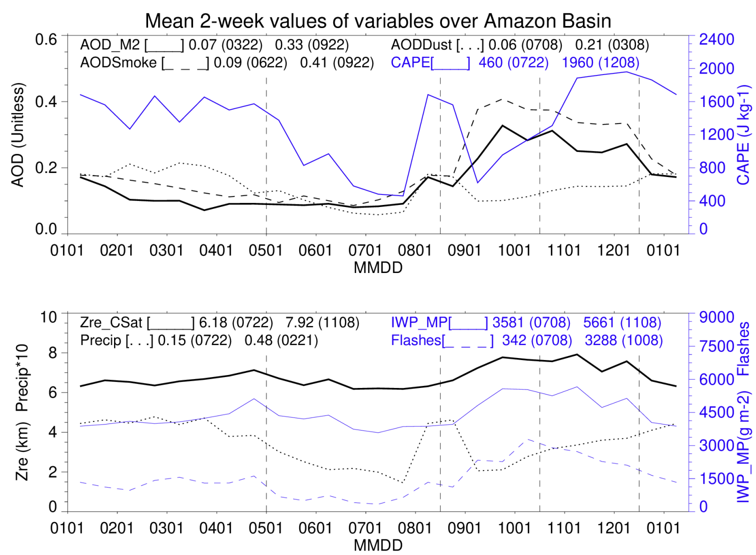

Figure 3. Time series showing bi-monthly mean values of MERRA-2 AOD (3a: solid black line), CALIOP AOD from dust (3a: dotted black line), CALIOP AOD from smoke (3a: dashed black line), ERA5 CAPE (3a: solid blue line), CloudSat Z_{re} (3b: solid black line), CloudSat and CALIPSO-based IWP (3b: solid blue line), IMERG precipitation (3b: dotted black line), and STARNET flashes (3b: dashed blue line). Time series created using observations on days in 2012-2017 with CloudSat and CALIPSO retrievals in Amazon Basin. Methods of obtaining daily values of AOD_Smoke and AOD_Dust described in section 2.2. Daily CAPE values obtained by taking 90th PCTL of three-hour maximum values (17-19 UT) over Basin. Daily flash values obtained by summing flashes over Basin during 10-minute time period that contains CloudSat overpass. Daily precipitation values are mean precipitation rates over Basin during 30-minute time periods containing CloudSat overpass. Daily AOD values are mean values over Basin during one-hour time period containing CloudSat overpass. Daily Z_{re} values are mean values of Z_{re} for deep convective systems observed that day over Basin. Daily IWP values obtained by taking maximum of mean IWP values for CloudSat-CALIPSO profiles of deep convective systems within Basin.

Figure 3a shows seasonal variations of CAPE and AOD; variables that affect the intensity of deep convection, while Figure 3b shows variations in metrics of convective intensity, specifically IWP, the centroid of Ze (Z_{re}), precipitation, and flashes. The mean values of CAPE range from 460 J kg^{-1} during July to 1960 J kg^{-1} at the beginning of the wet season in early December. In general, CAPE increases between July and December; however, it has a secondary peak during late August and early September, likely explaining a secondary maximum in precipitation observed during the same period. AOD is lowest during March and remains low through July. It then increases from August through September and remains high until the onset of the wet season in December. AOD from low-level smoke exceeds AOD from low-level dust by about 60%. Thus, the AOD seasonal cycle is driven by smoke, which is at a minimum in late June and maximizes in late September. The distributions of IWP and Z_{re} are very similar because the IWC values used in the integration to obtain IWP were derived from a combination of Z_e and the CALIPSO lidar attenuated backscatter (Deng et al., 2013). With the exception of rainfall, the convective intensity metrics have minima during the dry season (late July), increase through the early pre-monsoon period, and decrease slowly during the latter portion of the pre-monsoon season. Precipitation is also lowest during July, but it shows a broad maxima during the wet season and the aforementioned peak in late July and early August.

3.2 Sensitivity of precipitation and flash rates to CAPE and aerosol loading

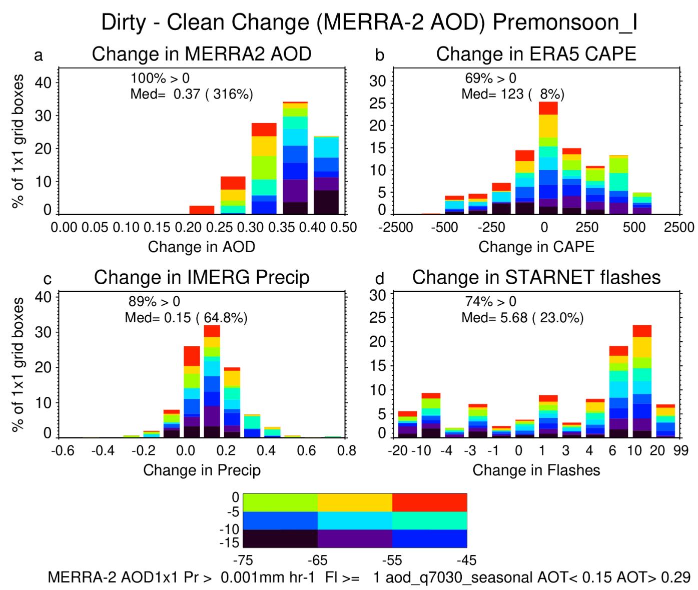

Figure 4. Probability distribution functions showing the percent of the 450 1° × 1° Amazon Basin grid boxes during August 16 – October 15 of 2012 - 2017 (pre-monsoon I) with changes in MERRA-2 AOD (a), ERA5 CAPE (b), IMERG precipitation (c), and STARNET flashes (d) between the ranges specified on the x axes between clean and dirty 30-minute periods. The colors show the contribution of each of the nine 10° in longitude × 5° in latitude regions to the overall change. Only periods with non-zero flashes and rainfall are considered. The percent changes are obtained by dividing the median difference of the quantity between the clean and dirty periods by the median value during the clean period.

Contrasts in AOD, CAPE, rain rate, and lightning flashes between 30-minute periods with low- and high-aerosol loading (clean and dirty periods) were examined for the pre-monsoon period using time series of MERRA-2 AOD, ERA5 CAPE, IMERG precipitation, and STARNET flashes for each of 450 1° × 1° grid boxes within the Amazon Basin. Time series of precipitation and flashes were calculated by averaging 0.1° × 0.1° gridded values over 30-minute periods. The archived temporal resolution of ERA5 CAPE and MERRA-2 AOD is one-hour. Values for 30-minute periods were obtained by replicating hourly values obtained by averaging values from ERA5 and MERRA-2 grid boxes within the 1° × 1° grid boxes. The resulting time series for each of the 450 grid boxes were then filtered to remove periods without flashes and also periods with precipitation rates of less than 0.001 mm $hour^{-1}$.

Figures 4a-d are probability distribution functions showing median changes in AOD, CAPE, precipitation, and lightning flashes between clean and dirty 30-minute periods during the pre-monsoon I (August 16 – October 15) time period. The analysis was limited to 30-minute periods with rain rates exceeding 0.001 mm hr^{-1} and flashes. Each bar shows the percent of the 450 1° × 1° grid boxes with changes between the values specified on the x-axes. The colors of the bars show the relative contribution of various 5° × 5° geographical regions to the total percent. The 30^{th} and 70^{th} percentiles of AOD over the Amazon Basin during these periods (0.15 and 0.29) were used as the thresholds between clean, moderate, and dirty periods (Altaratz et al., 2017). By definition, the change in AOD must be positive, as AOD was used in separating clean and dirty periods. Overall, the median AOD when dirty was 316% greater than the median AOD when clean. The median increase in CAPE between clean and dirty periods was a relatively small 123 J / kg (8%), with positive changes over 69% of the Basin. Overall, the median rain-rate increased by 0.15 mm hr^{-1} (65%), with 89% of the Basin having more rain when dirty. Increases in rain rate were greatest and most spatially coherent in the east-central portion of the domain (not shown). The median flash rate increased by a relatively modest 5.7 flashes (23%), with a large percentage (74%) of the Basin having more flashes when dirty. Increases in flash rate were greatest and mostly spatially coherent in the northern portion of the domain. The values quoted above were obtained using fields from all hours of the day. In order to determine if the results were an artifact caused by diel variations, the changes were also determined by sorting the fields into three-hour bins (00-03 UT, 03-06 UT, etc.) and re-calculating the changes. When this was done, the change in CAPE during the eight periods ranged from 69 to 157 J kg^{-1} (6-13%), the change in precipitation ranged from 0.08 to 0.16 mm hr^{-1} (59-108%), and the change in flashes ranged from 2.1 to 8.5 (16 – 32%). In order to test the sensitivity of the results to the method used to determine the aerosol thresholds, the changes were also determined using separate seasonal AOD thresholds for each grid box as opposed to one seasonal threshold for the Basin. When this was done, the median change in AOD was 0.34 (267%), the median change in CAPE was 44 J kg^{-1} (3%), with 56% of the domain having positive changes, the median change in precipitation was 0.13 mm hr^{-1} (54%) with 92% of the grid boxes having positive changes, and the median change in flashes was 4.2 (17%) with 70% of the grid boxes having positive changes. Thus, regardless of how the AOD threshold is specified, precipitation rates were 50-100% higher and flashes 15-30% higher during the mid-August to mid-October period when AOD was enhanced. The change in CAPE during this period was relatively modest (3-13%), suggesting that changes in AOD were responsible for much of the increases in precipitation and flashes.

The sensitivity of precipitation and flashes to aerosol loading was also examined during the latter portion of the pre-monsoon season (October 16 – December 15) and found to be less clear. During this period, the median change in AOD was 0.32 (287%), the median change in CAPE was 653 J kg^{-1} (52%), the median change in precipitation was 0.05 mm hr^{-1} (14.3%), and the median change in flashes was 2.1 (8.6%). Thus, during the pre-monsoon-II season, the main difference between the clean and dirty periods was a 52% increase in CAPE, which is certainly large enough to explain the modest increases in precipitation and flashes regardless of the aerosol loading. During this period, changes in precipitation and flashes were relatively modest, and hours with enhanced AOD often also had enhanced CAPE, making it impossible to detect an aerosol signal. The sensitivity of rain- and flash rates to aerosols during pre-monsoon I when the mean value of CAPE was 1067 J kg^{-1} but not pre-monsoon II when the mean value was 1788 J kg^{-1} (see Figure 3) suggests that convective intensity is more sensitive to aerosol loading when values of CAPE are relatively low.

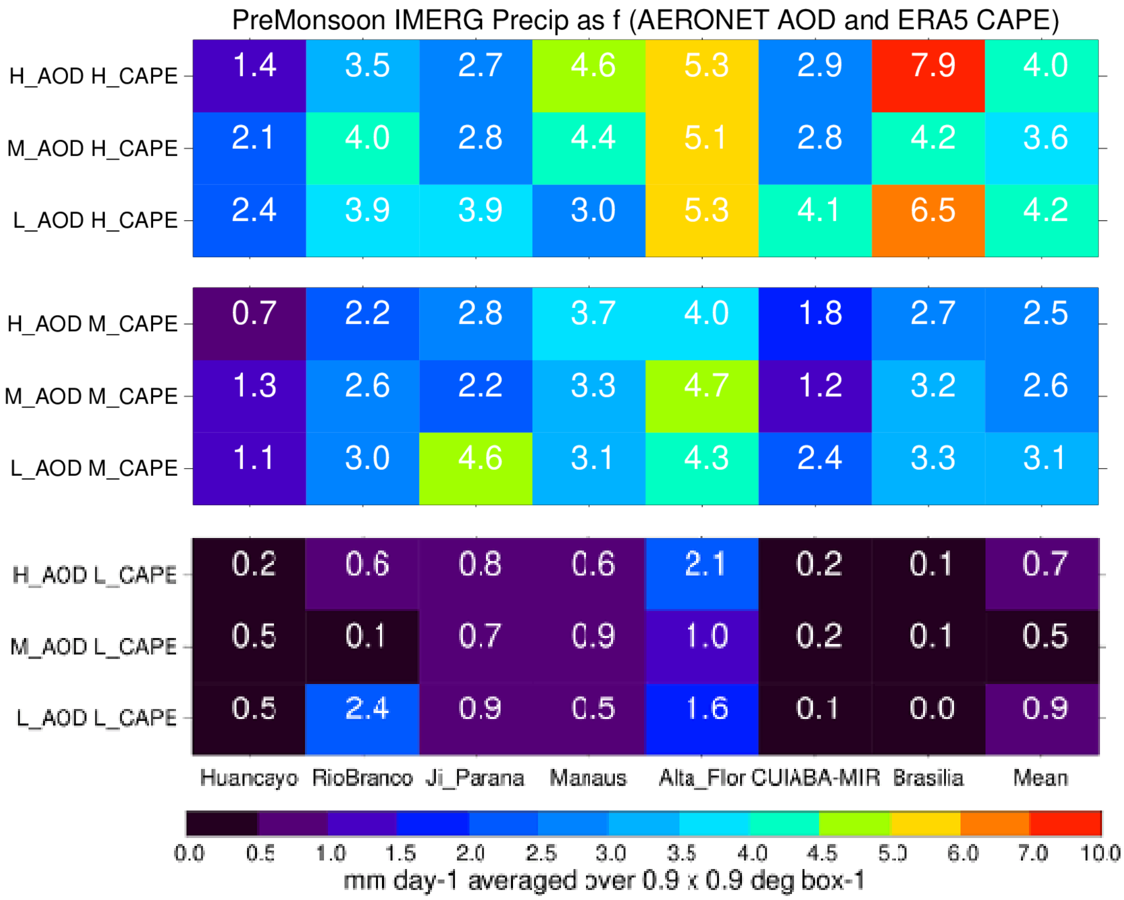

Figure 5. IMERG precipitation as a function of CAPE and AOD at each of the seven AERONET sites as well as the mean of the seven sites. Site-specific values of the 30th and 70th PCTLs of CAPE over the 12-18 UT period and AERONET AOD over the same period were used to partition days into nine bins containing low-, moderate-, and high values of CAPE and AOD (y-axis). Mean precipitation rates (mm day^{-1} averaged over 0.9° × 0.9° region) for each of these bins are shown for each site as well as the overall mean. The mean ratio of precipitation on high-CAPE days to low-CAPE days was 5.9, while the ratio of precipitation on high-AOD days to low-AOD days was 0.9.

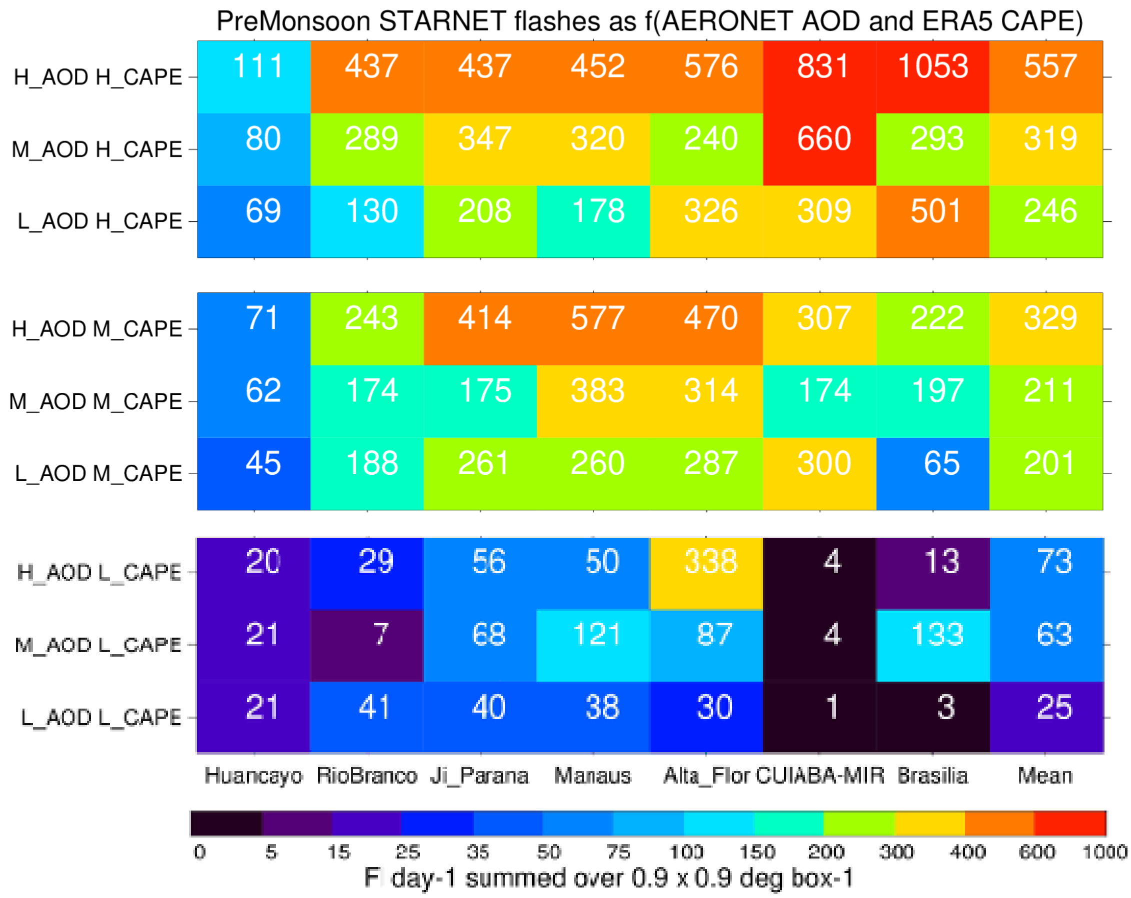

Figure 6. STARNET flashes for 0.9° × 0.9° regions containing each AERONET site plus the mean as a function of CAPE and AOD using the same bins as Figure 5. The mean ratio of flashes on high-CAPE days to low-CAPE days was 7.0, while the ratio of flashes on high-AOD days to low-AOD days was 2.0.

In order to further investigate the relationship between CAPE, AOD, precipitation, and flashes, the sensitivity of rain- and flash rates to CAPE and aerosol loading was examined for 0.9° × 0.9° regions centered on the AERONET sites (see Figure 1) using AOD measurements during the pre-monsoon time period. The unusually sized regions were chosen to be similar in size to the 1° × 1° regions used for our earlier analysis and are comprised of 81 0.1° × 0.1° grid boxes with the AERONET site in the middle. The ARM_Manacapuru, Manaus_EMBRAPA , and Amazon_ATTO_Tower sites are located close together and combined into a Greater Manaus data set for analysis. For each of the six actual sites and the Greater Manaus site (see Table 1), AOD measurements taken between 120000 (HHMMSS) UT and 175959 UT were read in and averaged to obtain representative values for each day. The daily values were then sorted with the highest 30% of the days at each site classified as high-AOD days, the lowest 30% classified as low-AOD days, and the remainder classified as moderate-AOD days (see Table 2). For each site, hourly values of CAPE were then extracted from ERA5 for 12-18 UT. Maxima of the seven hourly values were then determined for each day with AERONET data, and the maxima were sorted and binned in the same manner as the AOD to define low-CAPE, moderate-CAPE, and high-CAPE days. For each day, the STARNET flashes were summed and IMERG rain-rates were averaged over 0.9° × 0.9° regions centered on 0.1° × 0.1° grid boxes containing the sites to obtain representative values of precipitation and flashes.

Figures 5 and 6 show rain- and flash-rates for each of the nine AOD/CAPE bins. The values were constructed using observations during the pre-monsoon periods of 2012-2017. When controlling for AOD, precipitation increased by a factor of 3.9 between periods with low-and-moderate CAPE and by an additional factor of 1.4 between periods with moderate-and-high CAPE. The mean rain rate on high-CAPE days exceeded the mean rain rate on low-CAPE days by a factor of 5.9 with large regional variations, especially in the eastern Basin, near CUIABA-MIRANDA and Brasilia SONDA, where rain-rates were near zero on low-CAPE days but much higher on high-CAPE days resulting in extremely high ratios (see Table 3). The sensitivity of precipitation to AOD was relatively small with a factor of 2 site-to-site variations in the ratio between high-AOD and low-AOD periods that may be just noise. Specifically, the mean high-AOD to low-AOD precipitation ratio was 0.9, with values ranging from ~0.6 for southwestern sites (Huancayo-IGP, Rio Branco, Ji Parana, and CUAIBA-MIRANDA) to 1-1.3 for the other sites (Table 3). When the ratios were re-calculated using observations from the six-hour period (1500-2059 UT) with the most flashes, the dependence on CAPE increased, and a hint of a weak dependence on aerosol loading emerged. Specifically, the mean ratio of precipitation between high-CAPE and low-CAPE periods increased from 5.9 to 10, while the mean ratio of precipitation between low-AOD and high-AOD periods increased from 0.9 to 1.2.

In the mean, flashes increased by a factor of 7.0 between periods with low-CAPE and periods with high-CAPE with a factor of 4.6 increase between periods with low-and-moderate CAPE and an additional factor of 1.5 increase between periods with moderate-and-high CAPE. When controlling for CAPE, flashes increased by a factor of 1.3 between periods with low-and-moderate AOD and by an additional 1.6 between periods with moderate-and-high-AOD. The slightly larger percent increase between moderate-and-high AOD loading than between low-and-moderate is surprising as several studies show that flash rates tend to level off or decrease with AOD for larger values of AOD; however, the result may not be noise as it is supported by results at 4 of the sites (Rio Branco, Ji Parana SE, Alta Floresta, and Brasilia) and contradicted by results at only one of the sites (Manaus). The mean dependence of flash rate on AOD was largest for low values of CAPE; however, that result is driven by Alta Floresta, where the mean flash rate was a very high 338 flashes per day per 0.9° × 0.9° grid box when AOD and CAPE were high. When that site is excluded, the dependence of flash rate on AOD was actually largest on days with high CAPE. Flash rates on high-AOD days exceeded flash rates on low-AOD days at all seven sites, with the mean ratio equaling 2.0 and local ratios varying modestly from 1.5 at Huancayo-IGP to 2.3 for Greater Manaus and Brasilia SONDA (Table 3). When the ratios were re-calculated using observations from the six-hour period (1500-2059 UT) of highest flashes, the ratio of flashes between high-CAPE and low-CAPE days increased from 7.0 to 9.7 while the ratio of flashes between low-AOD and high-AOD days increased from 2.0 to 2.3. Thus, rain- and flash rates increase by a factor of 6-10 between low-CAPE and high-CAPE days. Flash rates are also sensitive to AOD increasing by approximately a factor of 2 at all sites between low-AOD and high-AOD days. However, precipitation response to AOD is mixed with increases more likely during periods and at locations where a relatively high percentage of the rain came from thunderstorms, such as the eastern portion of the domain and 15-21 UT.

Table 2. Mean 2012-2017 rainfall and flashes during the pre-monsoon period plus percentiles of CAPE and AOD used in classifying days as clean or dirty.

Site	Precip	Flashes	CAPE	CAPE	AOD	AOD
	Daily Mean mm 30 min^{-1} for 0.9° × 0.9° box that includes site	Daily mean total for the same box	PCTL30[a] J kg^{-1}	PCTL70[a] J kg^{-1}	PCTL30[a] Unitless	PCTL70[a] Unitless
Huancayo-IGP	1.1	56	8	812	0.07	0.12
Rio Branco	2.5	181	795	1813	0.21	0.45
Ji_Parana_SE	2.4	223	678	2102	0.24	0.53
Greater Manaus	2.7	264	661	1641	0.21	0.37
Alta Floresta	3.7	297	639	1985	0.25	0.51
CUIABA-MIRANDA	1.8	288	169	1530	0.21	0.47
Brasilia SONDA	3.1	276	2	1051	0.12	0.23

[a]PCTLxx refers to xx[th] percentiles of ERA-5 CAPE or AERONET AOD at each site

Table 3. Ratios of precipitation and flashes between periods with high-CAPE and low-CAPE and between periods with high-AOD and low-AOD

	High CAPE / Low CAPE (Unstable / Stable)[a]		High AOD / Low AOD (Dirty / Clean)[b]	
Site	Precipitation Ratio	Flash Ratio	Precipitation Ratio	Flash Ratio
Huancayo-IGP	5.1	4.3	0.57	1.5
Rio Branco	3.7	11	0.67	2.0
Ji_Parana_SE	3.9	6.1	0.67	1.8
Greater Manaus	6.1	4.6	1.3	2.3
Alta Floresta	3.3	2.5	1.0	2.2
CUIABA-MIRANDA	20.	200	0.72	1.9
Brasilia SONDA	81	12	1.1	2.3
Mean	5.9	7.0	0.89	2.0

[a]High (Low) CAPE days are days when CAPE exceeds (is less than) the 70[th] (30[th]) percentiles given in Table 2.
[b] High (Low) AOD days are days when AOD exceeds (is less than) the 70[th] (30[th]) percentiles given in Table 2.

3.3 Analysis using MERRA-2 AOD and CloudSat and CALIPSO profiles.

The effects of thermodynamics and microphysics on the vertical structure of deep convective events are now examined using median distributions of Z_e and mean distributions of IWC for deep convective systems sampled by CloudSat and CALIPSO over the Amazon Basin during the pre-monsoon period (see also Chen et al., 2016). As before, representative profiles are obtained after separating the profiles into three instability bins using 30th and 70th percentiles of ERA5 CAPE (990 and 1959 J kg^{-1}) and three aerosol-loading bins using 30th and 70th percentiles of total column MERRA-2 AOD (0.144 and 0.256). The methods used to obtain representative values of CAPE and AOD for each deep convective system are described in sections 2.3 and 2.4.

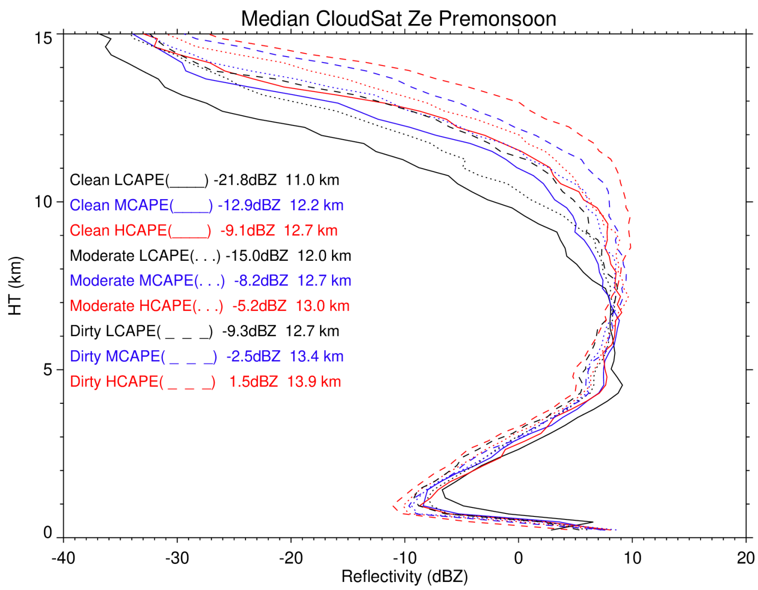

Figure 7. Median vertical profiles of Z_e (dBZ) for deep convective systems over the Amazon Basin during the pre-monsoon time period as a function of ERA5 CAPE and MERRA-2 AOD. The bins for CAPE are CAPE < 990 J / kg, 990 J / kg < CAPE < 1959 J / kg, and CAPE > 1959 J / kg). The bins for aerosol are AOD < 0.144, 0.144 < AOD < 0.256, and AOD > 0.256. For each of the bins, the mean value of Z_e between 11 and 14 kms (e.g., -21.8 dBZ for clean low-CAPE conditions) and the altitude of the -10 dBZ contour (e.g., 13.9 km for dirty high-CAPE conditions) are shown.

Figure 7 shows the median vertical profiles of Z_e for deep convective systems observed over the Amazon Basin during the pre-monsoon season. The figure contains nine Z_e profiles representing three-levels of instability based on CAPE and three-levels of aerosol loading based on AOD. The mean Z_e for all nine AOD / CAPE bins is ~ 8 dBZ at 7 km. The profiles diverge for altitudes above 7 km due to differences in hydrometeor loading and also because the radar signal in the upper troposphere is less subject to contamination via attenuation and multiple scattering (Protat et al., 2009). The mean Z_e for low-CAPE clean profiles decreases rapidly between 7 and 10 km, while the mean Z_e for high-CAPE dirty profiles increases slightly between 7 and 10 km. Profiles for intermediate levels of CAPE and AOD fall in between the extrema. The different behaviors arise from the sensitivity of the Z_e profile in the mixed phase region to hydrometeor size and phase. Specifically, Z_e is higher for water than for ice and higher for large hydrometeors such as hail or graupel than small hydrometeors. Zipser and Lutz (1994) found that vertical profiles of Z_e for tropical continental storms show a free-troposphere maxima and then decrease gradually with height above the freezing layer. In the mixed phase region, Heiblum et al. (2017) found that Z_e diminished by 3.5-5 dBZ / km over land where aerosols were plentiful. These Z_e profiles show maxima between 5 and 9 km and diminish by 1.3 dBZ / km between 8 and 11 km for dirty high-CAPE profiles to 5.5 dBZ / km between 8 and 11 km for clean low-CAPE profiles.

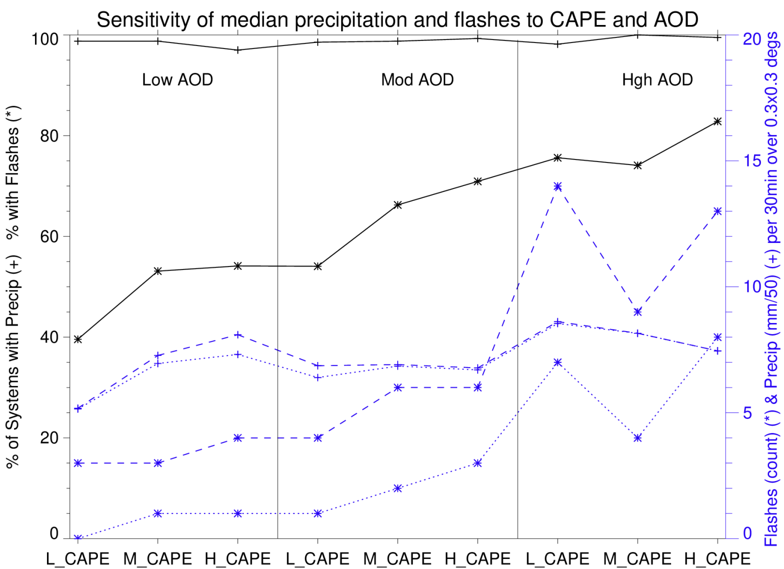

Figure 8. Rain- and flash-rates for low-, moderate-, and high- bins of CAPE and AOD. The solid black line with asterisks (pluses) shows the percent of deep convective systems with lightning (rain). The dashed blue line with asterisks shows the median flash count (30-minute sum of flashes over 0.3° × 0.3° region) for systems with non-zero flashes, while dotted blue line with asterisks shows median flash count for all systems. Dashed blue line with pluses shows median rain-rate (mm 30 min^{-1} averaged over a 0.3° × 0.3° region) for systems with non-zero flashes, while dotted blue line with asterisks shows the rain rate for all systems.

The mean value of Z_e in the 11-14 km range varied from -21.8 dBZ for clean low-CAPE profiles to 1.5 dBZ for dirty high-CAPE profiles. The altitude of the -10 dBZ contour is usually in this range and varies from 11.0 km for clean low-CAPE profiles to 13.9 km for dirty high-CAPE profiles. Controlling for CAPE, the increase in altitude from clean to dirty conditions averages 1.7 km for low values of CAPE and 1.2 km for moderate-and-high values of CAPE. Using the -10 dBZ contour as an estimate of the cloud top height and further assuming that flash rates are proportional to the 4.9^{th} power of cloud top height (Price and Rind, 1992), the 1.2-1.7 km difference in cloud height would correspond to a factor of 1.6-2.0 difference in flash rates between periods with low aerosol-loading and periods with high aerosol loading. Figure 8 shows rain- and flash-rate statistics for convective systems in each of the nine CAPE and AOD bins. These systems were almost always accompanied by rain; however, the percent with lightning varied from 40% for low-CAPE low-AOD conditions to 83% for high-CAPE high-AOD conditions. After controlling for CAPE, the percentage of systems with flashes increased from 49% for low-AOD conditions to 78% for high-AOD conditions. Similarly, the rain rate increased from 0.68 to 0.81 mm per 30 mins, and the flash count for flashing systems increased from 3.3 to 12.0 flashes per 30 minutes per 0.9 × 0.9° grid box. The factor of 3.6 increase in flashes is a factor of 2 larger than the expected value of 1.6-2.0 based on the differences in -10 dBZ heights between clean and dirty systems. This suggests that aerosol loading should also be considered when developing flash rate parameterizations for use in chemical transport and climate models (e.g., Stolz et al., 2017). The relationship between flashes and CAPE is noisier. The percent of deep convective systems with lightning increases with CAPE; however, flash rates of flashing storms were only weakly dependent on CAPE. Specifically, flash rates increased with CAPE for low- and moderate- values of AOD but decreased with CAPE for high values of AOD. The surprising results are likely noise, given the volatility of flash rates and the relatively small sample size.

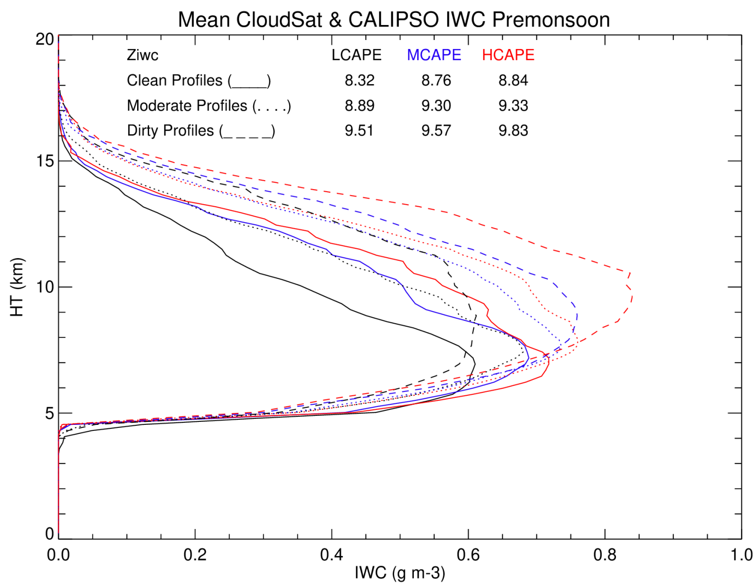

Figure 9. Mean vertical profiles of IWC for deep convective systems over the Amazon Basin during the pre-monsoon season with the same CAPE and AOD bins as in Figure 7. For each of the nine bins, the altitude of the Z_{IWC} centroid is shown.

Mean values of Z_e for all combinations of CAPE and AOD decrease with altitude between 11 and 14 km. The rate at which Z_e decreases is associated with the type and concentration of cloud ice particles in the region. Z_e is proportional to the 6th power of hydrometeor size, and large hydrometeors fall out of updrafts more rapidly than smaller hydrometeors (Dodson et al., 2018). Thus, IWC is highly correlated with Z_e (Heymsfield et al., 2016), with dirty high-CAPE profiles containing more ice likely as highly reflective hail or graupel (Dodson et al., 2018) than clean low-CAPE profiles. Mean vertical profiles of IWC for the nine CAPE/ AOD bins are shown in Figure 9. After controlling for CAPE, the higher mean values of Z_e and IWC for polluted conditions indicate that polluted storms contain stronger updrafts that are capable of transporting water droplets and large hydrometeors to higher altitudes (Chen et al., 2016; Morales-Rodriguez, 2019). The higher values also indicate that the aerosol availability for nucleation was large enough to keep the particle sizes small, allowing particles to be lofted as opposed to rained out. As expected from the Z_e profiles, mean IWC increases consistently with both CAPE and AOD. For example, between 7 and 15 km, IWC is clearly lowest for clean low-CAPE profiles and clearly highest for dirty high-CAPE profiles. At 10 km, the IWC under low-CAPE conditions equaled 0.30 g m^{-3} for clean conditions and 0.50 g m^{-3} for dirty conditions. Similarly, under moderate-CAPE conditions, IWC equaled 0.45 g m^{-3} and 0.65 g m^{-3}, while under high-CAPE conditions it equaled 0.50 g m^{-3} and 0.73 g m^{-3}. Thus, after controlling for CAPE, IWC increases by 45-70% between low and high-AOD conditions, with larger increases observed under low-CAPE conditions. The difference in IWC between clean low-CAPE profiles and dirty high-CAPE profiles is ~ a factor of 2.4, with mean IWC equaling 0.35 g m^{-3} for clean low-CAPE profiles and 0.83 g m^{-3} for dirty high-CAPE profiles. Z_{IWC} increases by 1.5 km (18%) between clean low-CAPE profiles and dirty high-CAPE profiles, 1.0 km (12%) between clean and dirty profiles, and 0.4 km (5%) between low- and high-CAPE profiles.

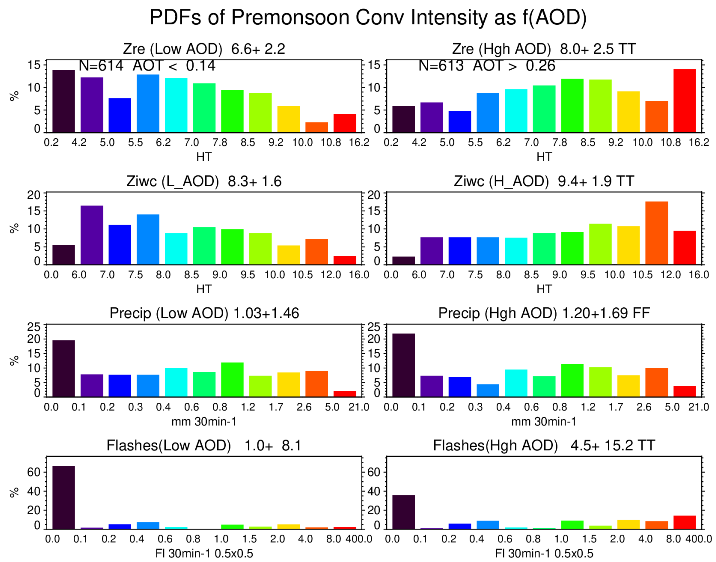

Figure 10. Probability distribution functions of Z_{re} (top row), Z_{IWC} (second row), rain rate (third row), and flash rate (bottom row) for pre-monsoon profiles sampled under low-aerosol loading (MERRA-2 AOD < 0.14) (left column) and high-aerosol loading (MERRA-2 AOD > 0.26) (right column). The mean and standard deviation are shown for each variable. TT indicates that the difference is significant at the 99% confidence level, while FF indicates that the difference is insignificant at the 95% confidence level.

Figure 10 compares the probability distribution functions of Z_{re}, Z_{IWC}, rain rate, and flash rate for deep convective systems sampled under low- and high-aerosol loading. The method used to obtain representative values of Z_{re} and Z_{IWC} for individual convective systems is discussed in section 2.1. For precipitation, the values shown are the means over the Amazon Basin of rain rates during the 30-minute period that contains the overpass. For flashes, the values shown are the means over the Amazon Basin of three ten-minute periods chosen so that the time of the overpass is in the middle period. The mean Z_{re} equals 6.6 $\pm$ 2.2 km for low AOD and 8.0 $\pm$ 2.5 km for high-AOD, a difference that is significant at the 99% confidence level (CL). Similarly, the mean Z_{IWC} equals 8.3 $\pm$ 1.6 km for low AOD and 9.4 $\pm$ 1.9 km for high AOD, a difference that is also significant at the 99% CL. The mean rain-rate increased from 1.03 $\pm$ 1.46 mm 30 min^{-1} for low-AOD conditions to 1.20 $\pm$ 1.69 mm 30 min^{-1} for high-AOD conditions, a 17% increase that was not significant at the 95% CL due to the high variability in precipitation rates. Finally, the mean flash rate increased from 1.0 $\pm$ 8.1 flashes per 0.5° × 0.5° grid box per 30-minutes for low-AOD conditions to 4.5 $\pm$ 15.2 flashes per 0.5° × 0.5° grid box per 30-minutes for high-AOD, a difference that is significant at the 99% CL despite the high variability in flash rates.

Q. Wang et al. (2018) found that flash rates in smoke-dominant regions of Africa were greater than in dust-dominated regions primarily because mid-level RH was 74 % in the smoke-dominant region and only 36% in the dust-dominant region. However, in this study, the mean RH in the mid-troposphere over the Amazon Basin was 74% for clean convective systems with fewer flashes and 65% for dirty convective systems with more flashes. The median lower troposphere static stability, i.e., the change in temperature between the surface and 700 hPa, was 17.2° C for clean systems and 18.7° C for dirty systems. Thus, the temperature fell off more rapidly with height when systems were dirty, indicating a more unstable environment. Thus, while the dirty profiles tended to have drier air in the mid-troposphere, which is a barrier to weak convection (Wall et al., 2015), the associated steeper lapse rates made the atmosphere more conducive to intense convection once the convective inhibition was overcome.

Table 4. Sensitivity of convective metrics to AOD after controlling for CAPE

	Low AOD (< 30^{th} PCTL)	High AOD (>70^{th} PCTL)	Significant Difference at 99% CL?	Significant Difference at 95% CL?
Z_{re} Low CAPE[a]	6.1 ± 2.1 (240)[b]	7.6 ± 2.6 (164)	Yes	Yes
Z_{re} Moderate CAPE	6.7 ± 2.2 (241)	6.9 ± 2.1 (251)	No	No
Z_{re} High CAPE	7.2 ± 2.2 (133)	8.4 ± 2.5 (198)	Yes	Yes
Z_{IWC} Low CAPE	7.9 ±1.6	9.1 ±2.0	Yes	Yes
Z_{IWC} Moderate CAPE	8.5 ±1.6	9.4 ±1.8	Yes	Yes
Z_{IWC} High CAPE	8.8 ±1.6	9.7 ±1.9	Yes	Yes
Precip Low CAPE	0.92 ±1.27	1.2 ±1.7	No	No
Precip Moderate CAPE	1.1 ±1.6	1.1 ±1.5	No	No
Precip High CAPE	1.2 ±1.5	1.3 ±1.9	No	No
Flashes Low CAPE	0.59 ± 2.0	7.0 ±26	Yes	Yes
Flashes Moderate CAPE	1.5 ±13	3.5 ±8.4	No	Yes
Flashes High CAPE	0.84 ± 2.0	3.7 ±7.1	Yes	Yes

[a]Units for Z_{re}, Z_{IWC}, precipitation, and flashes are km, km, mm 30 min^{-1}, and flashes per 0.5° × 0.5° grid box per 30-minutes

[b]Number of cases in each CAPE / AOD bin

In order to control for variations in thermodynamic forcing with AOD, we also examined variations in the centroid of Z_e (Z_{re}), and IWC (Z_{IWC}), precipitation rate, and flash rate with AOD after binning each variable into low-, moderate-, and high- CAPE bins (see Table 4). Increases in Z_{re}, Z_{IWC}, rain-rate, and flash-rate were still observed in all CAPE bins. As before, precipitation increased with AOD (0.08 – 0.30 mm 30 min^{-1}), but the increases were not significant at the 95% confidence level (CL). Increases in Z_{re} were significant for low- and high-CAPE bins but insignificant at the 95% CL for moderate levels of CAPE. Notably, the flash rate under low-CAPE conditions increased from 0.59 ± 2.0 flashes per 0.5° × 0.5° grid box per 30-minutes under low aerosol conditions to 7.0 ± 26 flashes per 0.5° × 0.5° grid box per 30-minutes under high-aerosol conditions (an increase by a factor of 11.8). Thus convective development and electrification appear to be especially sensitive to aerosol loading during periods with relatively low values of CAPE. That said, flash rates still increased by a factor of 2-4 between periods with low- and high-AOD when CAPE was moderate or high.

3.4 Sensitivity of flash rate to aerosol type

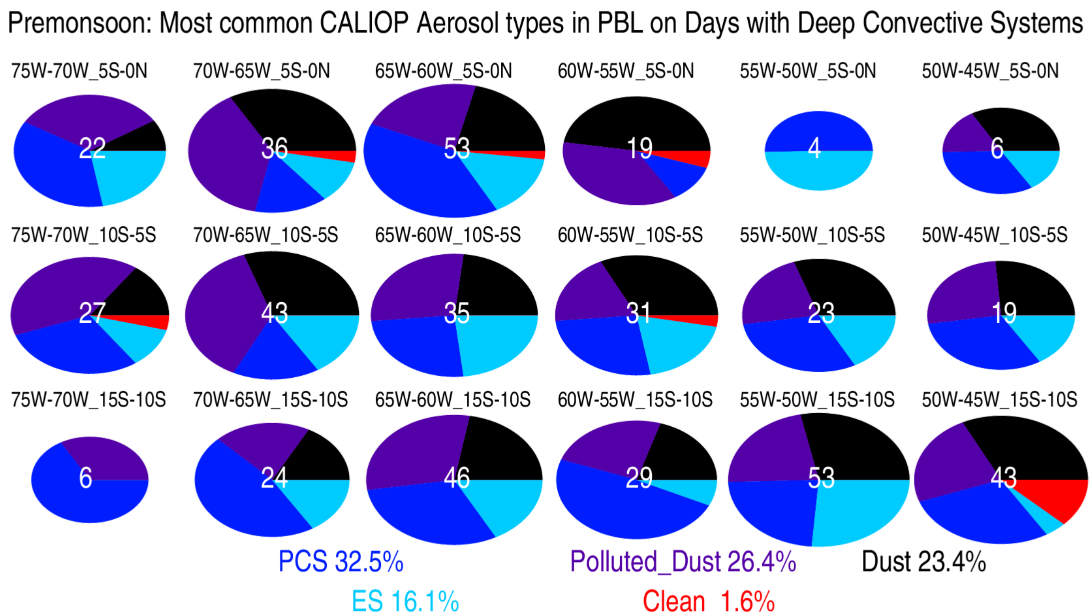

Figure 11. Pie charts showing regional variations in distribution of CALIOP aerosol types for deep convective systems observed during the pre-monsoon season. The number of systems for which typing was possible is shown in the center of each pie. The percent each type of system is shown at the bottom. The "Clean" aerosol type is essentially the Clean Continental category but it could include the Clean Marine type. To emphasize regional differences in the number of convective systems while maintaining readability, the radius of the pies varies with the number of observations divided by the maximum number of observations (53) to the power 0.2.

Prior studies have shown that the intensity of deep convective storms can be sensitive to aerosol type (Jiang et al., 2018; Yang et al., 2016). However, the effect of aerosol type on the intensity of deep convection is complex. When smoke is dominant, i.e., $\boldsymbol{\delta}_p$ is relatively small, the fine mode is dominant, and particles are mainly spherical, relatively small, and moderately absorbing. Yang et al. observed that the frequency, height, and flash rate associated with thunderstorms peaked on the weekend over central China, where aerosol absorption was strong, suppressing mid-week storms. But the peak occurred on weekdays over southeastern China where the aerosol single scattering albedo was much higher, lessening the aerosol radiative effect, and conditions were more humid, enhancing convective invigoration through the aerosol microphysical effect. Q. Wang et al. (2018) found that flash rates in smoke-dominant regions of Africa were greater than in dust-dominated regions primarily because mid-level RH was greater in the smoke-dominant region; however, aerosol type may also have played a role. Smoke aerosols are likely to absorb more than dust particles. While this absorption inhibits convection by decreasing the amount of radiation reaching the surface, it could also increase the intensity of convection as heating the aerosols layer destabilizes layers above the aerosol layer (Y. Wang et al., 2013).

In order to follow-up on these studies, we analyzed the lower tropospheric CALIOP aerosol type for the 1803 convective systems that occurred during the pre-monsoon season (see section 2.2). The aerosol type was identified for 519 systems, with 132, 144, 152, 81, and 10 systems identified as Dust, Polluted Dust, Polluted Continental Smoke, Elevated Smoke, and Clean (either Clean Continental or Clean Marine). The spatial distribution of the aerosol types for the systems is shown in Figure 11. Statistics for the systems classified as Dust, Polluted Dust, Polluted Continental Smoke, and Elevated Smoke are shown in Table 5. The sampled systems cover most of the Domain, suggesting that the statistics should be representative of a variety of environments despite regional variations in the frequency of convection and loss of data due to low-energy shots. Overall, the most common CALIOP aerosol type was Polluted Continental Smoke (152 cases; 32.5%), followed closely by Polluted Dust (144 cases; 26.4%) and Dust (132 cases; 23.4%). Elevated Smoke in the "lower troposphere" was also relatively common (81 cases; 16.1%) although the statistics for Elevated Smoke over-represent the southeast, specifically, 10-15° S and 55-50° W, where nearly 30% of the Elevated Smoke events occurred.

Table 5. Sensitivity of environmental and convective intensity variables to dominant CALIOP aerosol type in the lower troposphere (P > 675 hPa)

Variable	Units	Dust	Poll D	Poll C Smk	Elev Smk
# of Cases	Count	132	144	152	81
AOD	Unitless	0.221	0.275	0.251	0.358
CAPE	J kg^{-1}	1508	1766	1540	1822
Mid-RH	%	68.4	61.5	62.6	61.0
Z_{IWC}	km	8.56	8.85	9.06	9.17
Precip	mm 30 min^{-1}	0.74	0.80	1.20	1.39
Flashes	Count 30 min^{-1} 0.1° × 0.1° box^{-1}	1.16	2.47	4.79	3.54

In the mean, flash rates were 2-4 × higher when Polluted Continental Smoke (PCS) or Elevated Smoke (ES) was the most common CALIOP aerosol type as opposed to Dust or Polluted Dust (PD). However, none of these differences were significant at the 99% CL due to the limited sample sizes and large variability of flash rates. The flash rate when Dust was common was significantly less than the other rates at the 95% CL. Similarly, precipitation-rates were 50-90% greater when PCS or ES was the most common type as opposed to Dust or PD. The mean precipitation rates when Dust or PD was most common were statistically less than the precipitation rates when PCS (95 % CL) or ES (99% CL) was most common. The cause of the difference is likely related to differences in instability and aerosol loading rather than to differences in aerosol type. The "Dusty" period with low rain- and flash-rates was characterized by low mean values of MERRA-2 AOD (0.221), ERA5 CAPE (1508 J kg^{-1}), and high-values of mid-tropospheric RH (68.4%). This combination is often associated with less intense convection but not necessarily less rain. The "PD" period had moderate values of AOD (0.275), relatively high CAPE (1766 J kg^{-1}), and fairly low mid-tropospheric RH (61.5%). Precipitation-rates were similar to the Dusty period, but the systems were more intense with higher values of Z_{IWC} and flash rate. The PCS period had moderate values of AOD and CAPE but surprisingly intense convection with high values of Z_{IWC}, precipitation, and flashes. Interestingly, these results are consistent with Jiang et al. (2018), who observed higher values of Z_{IWC} over the Amazon under PCS-conditions as opposed to aerosol-free conditions. Finally, the "ES" period featured high mean values of CAPE and AOD. The elevated smoke may contribute to the larger rain- and flash-rates, but it may also be a consequence of additional lofting associated with higher-than-average values of CAPE.

4.0 Conclusions

In this study, the sensitivity of rain- and flash rates to instability and aerosol amount were examined over the Amazon Basin during the pre-monsoon season (August 16 – December 15) using metrics of convective intensity over deep convective scenes derived from CloudSat, total column AOD from AERONET and MERRA-2, aerosol types from CALIPSO, precipitation fields from IMERG, and flash rates from STARNET. The pre-monsoon season was chosen because it is a period with large variations in aerosols and the highest percentage of lightning-producing deep convective systems.

Initially, changes in CAPE, rain rate, and lightning flashes were examined as a function of aerosol loading using 24-hour time series of MERRA-2 AOD, ERA5 CAPE, IMERG precipitation, and STARNET flashes during the pre-monsoon I (August 16 – October 15) and pre-monsoon II (October 16 – December 15) time periods. During pre-monsoon I, precipitation rates were 50-100% higher and flashes 15-30% higher during hours with high-AOD than in hours with low AOD. The change in CAPE during this period was relatively modest, suggesting that changes in AOD were responsible for much of the increases in precipitation and flashes. The sensitivity of precipitation and flashes to aerosol loading was less clear during pre-monsoon II. During this period, changes in precipitation and flashes were small, and hours with enhanced AOD often also had enhanced CAPE, making it impossible to detect an aerosol signal. The sensitivity of rain- and flash-rates to aerosols during pre-monsoon I when CAPE is relatively low but not pre-monsoon II when CAPE is often high suggests that convective intensity may be more sensitive to aerosol loading when values of CAPE are relatively low.

The relationship between convective intensity and aerosol loading was then examined using AERONET AOD as a metric for aerosol loading and rain- and flash-rates for regions encompassing the AERONET sites. Both rain- and flash-rates increased by a factor of 5-10 between low-CAPE and high-CAPE days. Flash rates were also sensitive to AOD, increasing by approximately a factor of 2 at all sites between low-AOD and high-AOD days. The dependence of precipitation on AOD was more complex, but a weak positive relationship was found for times and regions when convective storms were common, specifically for afternoon hours and the eastern portion of the Basin.

Vertical profiles of radar reflectivity (Z_e) and IWC from CloudSat and CALIPSO were then used to examine the effects of thermodynamic and microphysical forcing on the structure of deep convective events. The values of Z_e diverged between 7 and 10 km, with Z_e decreasing rapidly for clean low-CAPE profiles but remaining steady for dirty high-CAPE profiles. This indicates that the vertical velocities in dirty-high CAPE environments were large enough to sustain a high concentration of larger hydrometeors, while vertical velocities in clean low-CAPE environments were insufficient to sustain high concentrations of larger hydrometeors. The cloud-top altitude was ~3 km higher for dirty high-CAPE storms than for clean low-CAPE storms. Controlling for CAPE, flash rates increased by more than a factor of 3 between clean and dirty periods, about twice as much as expected, given observed differences in convective cloud top heights. This suggests that aerosol loading should also be considered when developing flash rate parameterizations for use in chemical transport models and climate models. IWC increased by a factor of 2.4 between clean low-CAPE profiles and dirty high-CAPE profiles. Controlling for CAPE, IWC increased by 50-60%, and Z_{IWC} increased by 1.0 km between clean and dirty conditions.

The statistical significances of contrasts in Z_{re}, Z_{IWC}, rain-rate, and flash-rate between deep convective systems sampled under low- and high-aerosol loading were then examined. Z_{re} and Z_{IWC} increased by 1.4 and 1.1 km, respectively, differences that were significant at the 99% confidence level. The rain-rate increased by a modest 17%, an increase that was not significant at the 95% CI, while flash rates increased by 450%, an increase that was significant at the 99% confidence level. Thus, when individual convective systems were examined, as opposed to larger regions, e.g., $1^o \times 1^o$, the response of rain-rates to increasing AOD was fuzzier, possibly because focusing on an individual system emphasizes decreases in rain rate that may occur under high aerosol loading because droplets are too small to be rained out and are lofted into the mixed phase region. The contrast in mid-tropospheric RH and LTSS between clean and dirty periods was also examined. In general, the RH was lower in dirty systems, while the LTSS was larger. The lower RH and associated steeper lapse rates for dirty systems appear to make the atmosphere more conducive to intense convection and reinforce the large role thermodynamic forcing plays in determining the intensity of convection.

The sensitivity of flashes to the composition of aerosols was also examined. The most common CALIOP aerosol types associated with the deep convective systems observed in this study were Polluted Continental Smoke (33%), Polluted Dust (26%), Dust (23%), and Elevated Smoke (16%). Overall, the flash rate was 2-4 × greater when Elevated Smoke or Polluted Continental Smoke (i.e., smoke) was the main CALIOP aerosol type in the lower troposphere as opposed to Dust or Polluted Dust. The flash rates when smoke was present are likely higher because these periods also had higher values of CAPE and AOD and lower values of mid-tropospheric RH. However, it is possible that properties of the smoke, such as absorption and heating, played a role in the differences.

Acknowledgments

The authors acknowledge the support of NASA Grant 80NSSC20K0131 that was awarded to first author Dale Allen under the NASA ROSES-2018 CloudSat and CALIPSO solicitation. Ken Pickering, Siyu Shan, and Melody Avery were also supported under this grant. Z. Li was supported by the National Science Foundation (AGS2126098). In addition, co-author P. Artaxo acknowledges funding from FAPESP through grant 2017/17047-0.

Data Availability

CloudSat data were acquired via sftp from the CloudSat Data Processing Center (https://www.cloudsat.cira.colostate.edu/). CALIPSO data were acquired from the NASA EARTHDATA site (https://asdc.larc.nasa.gov/data/CALIPSO/). MERRA-2 AOD were accessed from https://gmao.gsfc.nasa.gov/reanalysis/MERRA-2/data_access/. ERA5 CAPE is available as part of the "ERA5 hourly data on single levels from 1940 to present" collection accessible at https://cds.climate.copernicus.eu/cdsapp#!/dataset/reanalysis-era5-single-levels?tab=form. Level 2 Spectral Deconvolution Algorithm (SDA) retrievals of AERONET AOD data for the Amazon Basin were obtained at https://aeronet.gsfc.nasa.gov/. IMERG precipitation data were accessed from the Goddard Earth Sciences Data and Information Center (GES DISC) at https://disc.gsfc.nasa.gov/datasets/GPM_3IMERGHH_06/summary?keywords=%22IMERG%20final%22 . STARNET data for the Amazon Basin were obtained from co-author Morales-Rodriguez.

The data sets and software needed to generate the plots and figures in the manuscript are archived on the Digital Repository at the University of Maryland (DRUM) at http://hdl.handle.net/1903/30416 . The research products archived in DRUM will be available indefinitely. The University of Maryland Libraries' DRUM repository is built on DSpace software, a widely used, reliable digital repository platform. DRUM performs nightly bit-level integrity tests on all files, and all contents are regularly copied to back-up storage. DRUM conforms to the digital preservation principles outlined in the University of Maryland Libraries' Digital Preservation Policy.

References

Albrecht, R. I., Morales, C.A. & Silva-Dias, M.A.F. (2011). Electrification of precipitating systems over the Amazon: Physical processes of thunderstorm development. *J. Geophys. Res*.,116, D08209. https://doi.org/10.1029/2010JD014756

Altaratz, O., Koren, I., Yair, Y., & Price, C. (2010). Lightning response to smoke from Amazonian fires. *Geophys Res Lett*, *37* (7). https://doi.org/10.1029/2010GL042679

Altaratz, O., Kucienska, B., Kostinski, A., Raga, G.B., & Koren, I. (2017). Global association of aerosol with flash density of intense lightning. *Environmental Research Letters*, 12 (11), 114037.

Andreae, M.O., Acevedo, O.C., Araùjo, A., Artaxo, P., Barbosa, C.G.G., Barbosa, H.M.J., et al. (2015). The Amazon Tall Tower Observatory (ATTO): overview of pilot measurements on ecosystem ecology, meteorology, trace gases, and aerosols. Atmospheric Chemistry and Physics, 15 (18), 10723–10776, https://doi.org/10.5194/acp-15-10723-2015

Andreae, M.O., Rosenfeld, D., Artaxo, P., Costa, A.A., Frank, G.P., Longo, K.M., & Silva-Dias, M.A.F. (2004). Smoking rain clouds over the Amazon. *Science*, 303(5662):1337-42.

Austin, R.T., Heymsfield, A.J., & Stephens, G.L. (2009). Retrieval of ice cloud microphysical parameters using the CloudSat millimeter-wave radar and temperature. *J. Geophys. Res*., 114, D00A23. doi:10.1029/2008JD010049

Artaxo, P., Vanderlei-Martins, J., Yamasoe, M.A., Procópio, A.S., Pauliquevis. T.M., Andrea, M.O., et al. (2002). Physical and chemical properties of aerosols in the wet and dry seasons in Rondônia, Amazonia. *J. Geophys. Res*., 107 (D20). https://doi.org/10.1029/2001JD000666.

Artaxo, P., Hansson, H.-C., Andreae, M.O., Bäck, J., Alves, E.G., Barbosa, H.M.J., et al. (2022). Tropical and Boreal Forest – Atmosphere Interactions: A Review. *Tellus B: Chemical and Physical Meteorology*, 74, 24–163. DOI: https://doi.org/10.16993/tellusb.34

Blyth, A.M., Christian, H.J., Driscoll, K., Gadian, A.M., & Latham, J. (2001). Determination of ice precipitation rates and thunderstorm anvil ice contents from satellite observations of lightning. *Atmos. Res*. 59-60, 217-229.

Buchard, V., Randles, C.A., da Silva, A.M., Darmenov, A., Colarco, P.R., Govindaraju, R., et al. (2017). The MERRA-2 aerosol reanalysis, 1980 - onward, Part 2: Evaluation and case studies. *Journal of Climate*, https://doi.org/10.1175/JCLI-D-16-0613.1

Buiat, M., Porcù, F., & Dietrich, S. (2017). Observing relationships between lightning and cloud profiles by means of a satellite-borne cloud radar. *Atmos. Meas. Tech*., 10, 221–230. https://doi.org/10.5194/amt-10-221-2017

Chen, T. Guo, J., Li, Z., Zhao, C., Liu, H., Cribb, M., et al. (2016). A CloudSat Perspective on the Cloud Climatology and Its Association with Aerosol Perturbations in the Vertical over Eastern China. *J. Atmos. Sci*, 73 (9), 3599-3616. https://doi.org/10.1175/JAS-D-15-0309.1

Chin, M., Ginoux, P., Kinne, S., Torres, O., Holben, B.N., Duncan, B.N., et al. (2002). Tropical aerosol optical thickness from the GOCART model and comparisons with satellite and sun photometer measurements. *J. Atmos. Sci.* 59 (3), 461-483. https://doi.org/10.1175/1520-0469(2002)059<0461:TAOTFT>2.0.CO;2

Choi, Y., Wang, Y., Zeng, T., Martin, R.V., Kurosu, T.P., & Chance, K. (2005). Evidence of lightning NOx and convective transport of pollutants in satellite observations over North America. *Geophys. Res. Lett*., 32, L02805. doi:10.1029/2004GL021436, 2005.

Cronk, H., & Partain, P. (2017). CloudSat ECMWF-AUX Auxiliary Data Product Process Description and Interface Control Document. http://www.cloudsat.cira.colostate.edu/sites/default/files/products/files/ECMWF-AUX_PDICD.P_R05.rev0_.pdf

Cummins, K.L., Murphy, M.J., Bardo, E.A., Hiscox, W.L., Pyle, R.B., & Pifer, A.E. (1998). A combined TOA/MDF Technology Upgrade of the US National Lightning Detection Network. *J. Geophys. Res*., 103 (D8), 9035-9044. https://doi.org/10.1029/98JD00153

Deng, M., Mace, G.G., Wang, Z.E., & Lawson, R.P. (2013). Evaluation of several A-Train Ice cloud retrieval products with in situ measurements collected during the SPARTICUS campaign.

J. of Applied Meteorology and Climatology, 52 (4), 1014-1030. https://doi.org/10.1175/JAMC-D-12-054.1

Deng, M., Mace, G.G., Wang, Z.E., & Berry, E. (2015). CloudSat 2C-ICE product update with a new Z(e) parameterization in lidar-only region. *J. Geophys. Res*., 120 (23). https://doi.org/10.1002/2015JD023600

Dodson, J.B., Taylor, P.C., & Branson, M. (2018). Microphysical variability of Amazonian deep convective cores observed by CloudSat and simulated by a multi-scale modeling framework. *Atmos. Chem. Phys*., 18 (9), 6493-6510. https://doi.org/10.5194/acp-18-6493-2018

Estevan, R., Martínez-Castro, D., Suarez-Salas, L., Moya, A., & Silva, Y. (2019). First two and a half years of aerosol measurements with an AERONET sunphotometer at the Huancayo Observatory, Peru. Atmospheric Environment: X (3), https://doi.org/10.1016/j.aeaoa.2019.100037

Fan, J. & Li, Z. (2022). Aerosol interaction with deep convection. *Aerosols and Climate*, 571-617. https://doi.org/10.1016/B978-0-12-819766-0.00001-8

Fan, J., Wang, Y., Rosenfeld, D., & Liu, X. (2016). Review of aerosol–cloud interactions: Mechanisms, significance, and challenges. *Journal of the Atmospheric Sciences*, 73(11), 4221–4252.

Fan, J., Rosenfeld, D., Zhang, Y., Giangrande, S.E., Li, Z., Machado, L.A., et al. (2018). Substantial convection and precipitation enhancement by ultrafine aerosol particles. Science, 359 (6374), 411-418. https://doi.org/10.1126/science.aan8461

Fan, J., Yuan, T., Comstock, J.M., Ghan, S., Khain, A., Leung, L.R., et al. (2009). Dominant role by vertical wind shear in regulating aerosol effects on deep convective clouds. *J. Geophys. Res*., 114, D22206. doi:10.1029/2009JD012352

Freud, E., & Rosenfeld, D. (2012). Linear relation between convective cloud drop number concentration and depth for rain initiation. *J. Geophys. Res.*, 117, D02207. doi:10.1029/2011JD016457

Freud, E., Rosenfeld, D., & Kulkarni, J.R. (2011). Resolving both entrainment-mixing and number of activated CCN in deep convective clouds. *Atmos. Chem. Phys.*, 11, 12,887–12,900. doi:10.5194/acp-11-12887-2011

Gelaro, R., McCarty, W., Suárez, M.J., Todling, R., Molod, A., Takacs, L., et. al. (2017). The modern-era retrospective analysis for research and applications, version 2 (MERRA-2). *J. Clim*. https://doi.org/10.1175/jcli-d-16-0758.1

Global Modeling and Assimilation Office (GMAO) (2015). MERRA-2 tavg1_2d_aer_Nx: 2d,1-Hourly,Time-averaged, Single-Level,Assimilation,Aerosol Diagnostics V5.12.4, Greenbelt, MD, USA, Goddard Earth Sciences Data and Information Services Center (GES DISC), Accessed: August 2022, 10.5067/KLICLTZ8EM9D

Grabowski, W.W., & Morrison, H. (2020). Do ultrafine cloud condensation nuclei invigorate deep convection. *Journal of the Atmospheric Sciences*, 77 (7), 2567-2583, https://doi.org/10.1175/JAS-D-20-0012.1

Guo, J., Deng, M., Lee, S.S., Wang, F., Li, Z., Zhai, P., et al. (2016). Delaying precipitation and lightning by air pollution over the Pearl River Delta, Part I: Observational Analyses. *J. Geophys. Res. Atmos*., 121, 6472-6488. https://doi.org/10.1002/2015JD023257

Heiblum, R., Koren, I., & Altaratz, O. (2012). New evidence of cloud invigoration from TRMM measurements of rain center of gravity. *Geophys. Res. Lett*., 39, L08803. https://doi.org/10.1029/2012GL051158

Heiblum, R.H., Koren, I., Altaratz, O., & Kostinski, A.B. (2017). The consistent behavior of tropical rain: Average reflectivity vertical profiles determined by rain top height. *Journal of Hydrometeorology*, 18 (3), 591– 609.

Hersbach, H., Bell, B., Berrisford, P., Hirahara, S., Horányi, A., Muñoz-Sabater, J. et al. (2020). The ERA5 global reanalysis. *Quarterly Journal of the Royal Meteorological Society*. https://doi.org/10.1002/qj.3803

Heymsfield, A.J., Matrosov, S.Y., & Wood, N.B. (2016). Toward improving ice water content and snow-rate retrievals from radars. Part I: X and W bands, emphasizing CloudSat. *J. of Appl. Met. And Clim*., 5 (9), 2063-2090. https://doi.org/10.1175/JAMC-D-15-0290.1

Hollingsworth, A., Engelen, R.J., Textor, C., Benedetti, A., Boucher, O., Chevallier, F., et al. (2008). Toward a monitoring and forecasting system for atmospheric composition. *Bull. Am. Meteorol. Soc*., 89, 1147-1164.

Holben, B. N., Tanré, D., Smirnov, A., Eck, T., Slutsker, I., Abuhassan, N., et al. (2001). An emerging ground-based aerosol climatology: Aerosol optical depth from AERONET. *J. Geophys. Res*., 106, 12067–12097. https://doi.org/10.1029/2001JD900014

Huffman, G.J., Bolvin, D.T., Braithwaite, D., Hsu, K., Joyce, R., Kidd, C., et al. (2020). Integrated Multi-satellitE Retrievals for the Global Precipitation Measurement (GPM) mission (IMERG). Chapter 19 in *Adv. Global Change Res., Vol. 67*, *Satellite Precipitation Measurement*, V. Levizzani, C. Kidd, D. Kirschbaum, C. Kummerow, K. Nakamura, F.J. Turk (Ed.), Springer Nature, Dordrecht, ISBN 978-3-030-24567-2 / 978-3-030-24568-9 (eBook), 343-353. https://doi.org/10.1007/978-3-030-24568-9_19

Huffman, G.J., Bolvin, D.T., Braithwaite, D., Hsu, K., Joyce, R., Kidd, C., et al. (2019). Algorithm Theoretical Basis Document (ATBD) Version 5.2 for the NASA Global Precipitation Measurement (GPM) Integrated Multi-satellitE Retrievals for GPM (I-MERG). GPM Project, Greenbelt, MD, 38 pp.

Hunt, W.H., Winker, D.M., Vaughan, M.A., Powell, K.A., Lucker, P.L., & Weimer, C. (2009). CALIPSO lidar description and performance assessment. *J. Atmos. Oceanic Technol.*, *26*(7), 1214–1228. https://doi.org/10.1175/2009JTECHA1223.1

Jiang, H.J., Su, H., Huang, L., Wang, Y., Massie, S., Zhao, B., Omar, A., & Wang, Z. (2018). Contrasting effects on deep convective clouds by different types of aerosols. *Nature Communications*, 9. https://doi.10.1038/s41467-018-06280-4

Kahn, R.A., Gaitley, B.J., Martonchik, J.V., Diner, D.J., Crean, K.A., & Holben, H. (2005). Multiangle Imaging Spectroradiometer (MISR) global aerosol optical depth validation based on 2 years of coincident Aerosol Robotic Network (AERONET) observations. *J. Geophys. Res.*, 110, D10S04. https://doi.org/10.1029/2004JD004706

Khain, A. (2009). Notes on state-of-the-art investigations of aerosol effects on precipitation: A critical review. *Environ. Res. Lett.*, 4, 015004.

Khain, A., Rosenfeld, D., & Pokrovsky, A. (2005). Aerosol impact on the dynamics and microphysics of deep convective clouds. *Q. J. R. Meteorol. Soc.*, 131, 2639-2663.

Kim, M.-H., Omar, A.H., Tackett, J.L., Vaughan, M.A., Winker, D.M., Trepte, C.R., et al. (2018). The CALIPSO version 4 automated aerosol classification and lidar ratio selection algorithm. *Atmos. Meas. Tech.*, 11, 6107–6135. https://doi.org/10.5194/amt-11-6107-2018

Koren, I., Feingold, G., & Remer, L.A. (2010). The invigoration of deep convective clouds over the Atlantic: aerosol effect, meteorology or retrieval artifact. *Atmos. Chem. Phys.*, 10, 8855-8872. https://doi.org/10.5194/acp-10-8855-2010

Koren, I., Kaufman, Y.J., Rosenfeld, D., Remer, L.A., & Rudich, Y. (2005). Aerosol invigoration and restructuring of Atlantic convective clouds. *Geophys. Res. Lett.*, 32, L14828. https://doi.org/10.1029/2005GL023187

Koren, I., Martins, J.V., Remer, L.A., & Afargan, H. (2008). Smoke invigoration versus inhibition of clouds over the Amazon. *Science*, 321, 946-949.

Kumar, S., Flores, J.L., Moya-Álvarez, A.S., Martinez-Castro, D., & Silva, Y. (2023). Characteristics of cloud properties over South America and over Andes observed using CloudSat and reanalysis data. *International Journal of Remote Sensing*, 44 (6), 1976-2004. https://doi.org/10.1080/01431161.2023.2193301

Lee, S.-S., Guo, J., & Li, Z. (2016). Delaying precipitation by air pollution over the Pearl River Delta. Part II: Model simulations. *J. Geophys. Res. – Atmos.*, 121 (19), 11,739-11,760. https://doi.org/10.1002/2015JD024362

Li, Z., Rosenfeld, D., & Fan, J. (2017). Aerosols and their impact on radiation, clouds, precipitation, and severe weather events. *Oxford Research Encyclopedias*. https://doi.org/10.1093/acrefore/9780199389414.013.126

Liu, N., Liu, C., Chen, B., & Zipser, E. (2020). What are the favorable large-scale environments for the highest-flash-rate thunderstorms on Earth. *Journal of the Atmospheric Sciences,* 77(5), 1583-1612. https://doi.org/10.1175/JAS-D-19-0235.1

Liu, Y., Guha, A., Said, R., Williams, E., Lapierre, J., Stock, M., & Heckman, S. (2020). Aerosol effects on lightning characteristics: A comparison of polluted and clean regimes. *Geophysical Research Letters*, 47, e2019GL086825. https://doi.org/10.1029/2019GL086825

Liu, Z., Kar, J., Zeng, S., Tackett, J., Vaughan, M., Avery, M., et al. (2018). Discriminating Between Clouds and Aerosols in the CALIOP Version 4.1 Data Products. *Atmos. Meas. Tech*, 12, 703-734. https://doi.org/10.5194/amt-12-03-2019

Lohmann, U. (2008). Global anthropogenic aerosol effects on convective clouds in ECHAM5-HAM. *Atmos. Chem. Phys*., 8, 2115-2131.

Mace, G.G., & Zhang, Q. (2014). The CloudSat radar-lidar geometrical profile product (RL-GeoProf); Updates, improvements and selected results. *J. Geophys. Res*., 119. https://doi.org/10.1002/2013JD021374

McFiggans, G., Artaxo, P., Baltensperger, U., Coe., H., Facchini, C., Feingold, G. et al. (2006). The effect of physical & chemical aerosol properties on warm cloud droplet activation. *Atmos. Chem. Phys.*, 6, 2593–2649, www.atmos-chem-phys.net/6/2593/2006/, doi:10.5194/acp-6-2593-2006.

Manoj, M.G., Lee, S.-S., & Li, Z. (2021). Competing aerosol effects in triggering deep convection over the Indian Region. *Clim. Dyn.*, 56, 1815-1835. https://doi.org/10.1007/s00382-020-05561-3

Marchand, R., Mace, G.G., Ackerman, T., & Stephens, G. (2008). Hydrometeor Detection using CloudSat-an Earth Orbiting 94-GHz Cloud Radar. *J. Atmos. Oceanic Technol*., 25, 519-533.

Marengo, J.A., Liebmann, B., Kousky, V.E., Filizola, N.P., & Wainer, I.C. (2001). Onset and end of the rainy season in the Brazilian Amazon Basin. *Journal of Climate*, 14(5), 833-852, https://doi.org/10.1175/1520-0442(2001)014%3C0833:OAEOTR%3E2.0.CO;2

Martin, S.T., Artaxo, P., Machado, L., Manzi, A.O., Souza, R.A.F., Schumacher, C., et al. (2017). The Green Ocean Amazon Experiment (GoAmazon2014/5) observes pollution affecting gases, aerosols, clouds, and rainfall over the rain forest. Bulletin of the American Meteorological Society, 981-997, https://doi.org/10.1175/BAMS-D-15-00221.1

Mataveli, G.A.V., de Oliveira, G., Seixas, H.T., Pereira, G., Stark, S.C., Gatti, L.V., et al. (2021). Relationship between Biomass Burning Emissions and Deforestation in Amazonia over the Last Two Decades. *Forests*, 12 (9), 1217, https://doi.org/10.3390/f12091217

Mielonen, T., Arola, A., Komppula, M., Kukkonen, J.; Koskinen, J., De Leeuw, G., & Lehtinen, K.E.J. (2009). Comparison of CALIOP level 2 aerosol subtypes to aerosol types derived from AERONET inversion data. *Geophys. Res. Lett.*, 36 (18), **https://doi.org/10.1029/2009GL039609**

Morales-Rodriguez, C.A. (2019). Thunderstorm efficiency regimes in South America as observed by STARNET and TRMM. *J. Geophys. Res. Atmos.*, 124 (21), 11428-11451. https://doi.org/10.1029/2019JD030950

Morales-Rodriguez, C.A., Neves, J.R., & Anselmo, E. (2011). Sferics Timing and Ranging Network – STARNET: Evaluation over South America. *Proceedings of the 14th International Conference on Atmospheric Electricity* – ICAE, Rio de Janeiro, Brazil.

Morales-Rodriguez, C.A., Neves, J.R., Anselmo, E.M., Camara, K.S., Barreto, W., Paiva, V., & Holle, R.L. (2014). 8 years of Sferics Timing and Ranging NETwork -STARNET: A lightning climatology over South America, *23rd International Lightning Detection Conference,* Tucson, Arizona.

Niu, F., & Li, Z. (2012). Systematic variations of cloud top temperature and precipitation rate with aerosols over the global tropics. *Atmos. Chem. Phys.,* 12, 8491-8498. https://doi.org/10.5194/acp-12-8491-2012

Palacios, R.D., Artaxo, P., Cirino, G.G., Nakale, V., Morais, F.G., Rothmund, L.D., et al. (2022). Long-term measurements of aerosol optical properties and radiative forcing (2012-2017) over Central Amazonia. *Atmósfera*, 35(1), 143-163. https://doi.org/10.20937/ATM.52892

Papagiannopoulos, N., Mona, L., Alados-Arboledas, L., Amiridis, V., Baars, H., Binietoglou, I., et al. (2016). CALIPSO climatological products: Evaluation and suggestions from EARLINET *Atmospheric Chemistry and Physics*, 16 (4), 2341–2357. https://doi.org/10.5194/acp-16-2341-2016

Peng, J., Li, Z., Zhang, H., Liu, J., & Cribb, M.C. (2016). Systematic changes in cloud radiative forcing with aerosol loading for deep clouds from multi-year global A-Train satellite datasets. *J. Atmos. Sci.*, 73, 231-249. https://doi.org/10.1175/JAS-D-15-0080.1

Petersen, W.A., & Rutledge, S.A. (2001). Regional variability in tropical convection: Observations from TRMM, *J. Climate*, 14, 3566-3586.

Price, C., & Rind, D. (1992). A simple lightning parameterization for calculating global lightning distributions. *J. Geophys. Res.*, **97**, 9919-9933. https://doi.org/10.1029/92JD00719

Protat, A., Bouniol, D., Delanoë, J., O'Connor, E., May, P.T., Plana-Fattori, et al. (2009). Assessment of Cloudsat Reflectivity Measurements and Ice Cloud Properties Using Ground-Based and Airborne Cloud Radar Observations. *J. Atmos. Oceanic Technol.*, 26, 1717–1741. http://dx.doi.org/10.1175/2009JTECHA1246.1

Randles, C.A., da Silva, A.M., Buchard, V., Colarco, P.R., Darmenov, A., & Govindaraju, R., et al. (2017). The MERRA-2 Aerosol Reanalysis, 1989-onward, Part I: System Description and Data Assimilation Evaluation. *J. Climate*, 30(17), 6823-6850. https://doi.org/10.1175/JCLI-D-16-0609.1

Remer, L.A., Kleidman, R.G., Levy, R.C., Kaufman, Y.J., Tanre, D., Mattoo, S., et al. (2008). Global aerosol climatology from the MODIS satellite sensors. *J. Geophys. Res*., 113, D14S07. https://doi.org/10.1029/2007JD009661

Romps, D.M., Seeley, J.T., Vollaro, D., & Molinari, J. (2014). Projected increase in lightning strikes in the United States due to global warming. *Science,* 346 (6211), 851-854. https://doi.org/10.1126/science.1259100

Rosenfeld, D. (1999). TRMM observed first direct evidence of smoke from forest fires inhibiting rainfall. *Geophys. Res. Lett*., 26(20), 3105–3108. https://doi.org/10.1029/1999GL006066

Rosenfeld, D., Woodley, W.L., Lerner, A., Kelman, G., & Lindsey, D.T. (2008). Satellite detection of severe convective storms by their retrieved vertical profiles of cloud particle effective radius and thermodynamic phase. *J. Geophys. Res.*, 113, D04208. https://doi.org/10.1029/2007JD008600

Saad, S.I., da Rocha, H.R., Silva-Dias, M.A.F., & Rosolem, R. (2010). Can the deforestation breeze change the rainfall in Amazonia? A case study for the BR-163 highway region. *Earth Interactions*, 14 (18). https://doi.org/10.1175/2010EI351.1

Saraiva, I., Dias, M.A.F., Morales, C.A.R., & Saraiva, J.M.B. (2017). Regional variability of rain clouds in the Amazon Basin as seen by a network of weather radars. *Journal of Applied Meteorology and Climatology*, 55 (12), 2657-2675. https://doi.org/10.1175/JAMC-D-15-0183.1

Sassen, K., & Wang, Z. (2008). Classifying clouds around the globe with the CloudSat radar: 1-year of results. *Geophys. Res. Lett*., 35, L04805. https://doi.org/10.1029/2007GL032591

Saunders, C.P.R., Bax-norman, H., Emersic, C., Avila, E.E., & Castellano, N.E. (2006). Laboratory studies of the effect of cloud conditions on graupel/crystal charge transfer in thunderstorm electrification. *Quarterly Journal of the Royal Meteorological Society*, 132 (621), 2653-2673. https://doi.org/10.1256/qj.05.218.

Schafer, J.S., Eck, T.F., Holben, B.N., Artaxo, P., & Duarte, A.F. (2008). Characterization of the optical properties of aerosols in Amazonia from long-term AERONET monitoring (1993-1995 and 1999-2006). *J. Geophys. Res*., 113 (D4). https://doi.org/10.1029/2007JD009319

Stephens, G.L., Vane, D.G., Boain, R.J., Mace, G.G., Sassen, K., Wang, Z., et al. (2002). The CloudSat mission and the A-Train: A new dimension of space-based observations of clouds and precipitation. *Bull. Of Amer. Met. Soc.*, *83*(12), 1771-1790.

Storer, R.L., van den Heever, S.C., & L'Ecuyer, T.S. (2014). Observations of aerosol-induced convective invigoration in the tropical east Atlantic. *J. Geophys. Res. Atmos*., 119, 3963–3975, doi:10.1002/2013JD020272

Stolz, D.C., Rutledge, S.A., & Pierce, J.R. (2015). Simultaneous influences of thermodynamics and aerosols on deep convection and lightning in the tropics. *J. Geophys. Res. Atmos.*, 120 (12), 6207-6231. https://doi.org/10.1002/2014JD023033

Stolz, D.C., Rutledge, S.A., Piece, J.R., & van den Heever, S.C. (2017). A global lightning parameterization based on statistical relationships among environmental factors, aerosols, and convective clouds in the TRMM climatology, *J. Geophys. Res. Atmos*., 122 (14), 7461-7492, https://doi.org/10.1002/2016JD026220

Tacket, J.L., Ryan R., Vaughan, M.A., Garnier, A., Getzewich, B., Winker, D., & Trepte, C. (2022). Mitigation Strategy for the Impact of Low Energy Laser Pulses in CALIOP Calibration and Level 2 Retrievals. NTRS-NASA Technical Report 20220006725, 30th International Laser Radar Conference. https://ntrs.nasa.gov/citations/20220006725

Tackett, J.L., Winkler, D.M., Getzewich, B.J., Vaughan, M.A., Young, S.A., & Kar, J. (2018). CALIPSO lidar level 3 aerosol profile product: version 3 algorithm design. *Atmos. Meas. Tech.*, 11, 4129-4152. https://doi.org/10.5194/amt-11-4129-2018

Takahashi, T. (1978). Riming electrification as a charge generation mechanism in thunderstorms. *Journal of the Atmospheric Sciences*, *35*(8), 1536-1548.

Tanelli, S., Durden, S.L., Im, E., Pak, K.S., Reinke, G.D., Partain, Haynes, J.M., & Marchand, R.T. (2008). CloudSat's cloud profiling radar after two years in orbit: performance, calibration, and processing. *Geoscience and Remote Sensing IEEE Transactions on,* 46(11), 3560-3573.

Tao, W.K., Chen, J.P., Li, Z., Wang, C., & Zhang, C. (2012). Impact of aerosols on convective clouds and precipitation. *Reviews of Geophysics*, *50*(2). https://doi.org/10.1029/2011RG000369

Ter Steege, H., Pitman, N.C.A., Sabatier, D., Baralot, C., Salomão R.P., Guevera, J.E., et al. (2013). Hyperdominance in the Amazonian Tree Flora. *Science,* 342(6156). https://doi.org/10.1126/science.1243092

Vaughan, M.A., Powell, K.A., Winkler, D.M., Hostetler, C.A., Kuehn, R.E., Hunt, W.H., et al. (2009). Fully Automated Detection of Cloud and Aerosol Layers in the CALIPSO Lidar Measurements. *J. Atmos. Oceanic Technol.*, 26, 2034–2050. doi: http://dx.doi.org/10.1175/2009JTECHA1228.1

Veals, P.G., Varble, A.C., Russell, J.O., Hardin, J.C., & Zipser, E.J. (2021). Indications of a decrease in the depth of deep convective cores with increasing aerosol concentration during the CACTI campaign. *Journal of the Atmospheric Sciences*, 79 (3), 705-722. https://doi.org/10.1175/JAS-D-21-0119.1

Virts, K.S., Wallace, J.M., Hutchins, M.L., & Holzworth, R.H. (2013). Highlights of a new ground-based, hourly global lightning climatology. *Bulletin of the American Meteorological Society*, 94, 1381-1392.

Wall, C., Zipser, E., & Lin, C. (2014). An Investigation of the Aerosol Indirect Effect on Convective Intensity Using Satellite Observations. *J. Atmos. Sci.*, 71, 430–447. doi: http://dx.doi.org/10.1175/JAS-D-13-0158.1

Wang, Q., Li, Z., Guo, J., Zhao, C., & Cribb, M. (2018). The Climate Impact of Aerosols on the Lightning Flash Rate: Is it Detectable from Long-term Measurements? *Atmos. Chem. Phys.*, 18, 12797-12816. https://doi.org/10.5194/acp-18-12797-2018

Wang, Y., Khalizov, A., Levy, M., & Zhang, R. (2013). New directions: light absorbing aerosols and their atmospheric impacts. *Atmos. Environ.* 2013;81:713–715. https://doi.org/10.1016/j.atmosenv.2013.09.034

Williams E.R., Rosenfeld, D., Madden, N., Gerlach, J., Gears, N., Atkinson, L., et al. (2002). Contrasting convective regimes over the Amazon: Implications for cloud electrification. *J. Geophys. Res.*, 107 (D20), 8082. https://doi.org/10.1029/2001JD000380

Winker, D.M.,Vaughan, M.A., Omar, A., Hu, Y., Powell, K.A., Liu, Z., et al. (2009). Overview of the CALIPSO mission and CALIOP data processing algorithms. *Journal of Atmospheric and Oceanic Technology*, 26 (11), 2310-2323.

Winker, D.M., Pelon, J., Coakley Jr., J.A., Ackerman, S.A., Charlson, R.J., & Colarco, P.R., et al. (2010). The CALIPSO Mission, A global 3-d view of aerosols and clouds. *Bull. of the American. Met. Soc.,* 91 (9), 1211-1230. https://doi.org/10.1175/2010BAMS3009.1

Wu, M., & Lee, J.-E. (2019). Thresholds for atmospheric convection in Amazonian rainforests. *Geophysical Research Letters*, 46(16), 10024-10033. https://doi.org/10.1029/2019GL082909

Wunderling, N., Staal, A., Sakschewski, B., & Winkelmann, R. (2022). Recurrent droughts increase risk of cascading tipping events by outpacing adaptive capacities in the Amazon rain forest. *Proceedings of the National Academy of Sciences (PNAS)*, 119 (32). https://doi.org/10.1073/pnas.2120777119

Yang, X., & Li, Z. (2014). Increases in thunderstorm activity and relationships with air pollution in southeast China. *J. Geophys. Res. Atmos.*, 119, 1835–1844. https://doi.org/10.1002/2013JD021224

Yang, X., Li, Z., Liu, L., Zhou, L., Cribb, M., & Zhang, F. (2016). Distinct weekly cycles of thunderstorms and a potential connection with aerosol type in China. *Geophys. Res. Lett*., 43. https://doi.org/10.1002/2016GL070375

Yang, X., Yao, Z., & Li, Z. (2013). Heavy air pollution suppresses summer thunderstorms in central China. *J. Atmos. & Solar-Terrestrial Phys*., 95-96, 28-40. https://doi.org/10.1016/j.jastp.2012.12.023

Young, S.A., Vaughan, M.A., Garnier, A., Tackett, J. L., Lambeth, J.B., & Powell, K.A. (2018). Extinction and Optical Depth Retrievals for CALIPSO's Version 4 Data Release. *Atmos. Meas. Tech.*, 11, 5701-5727. https://doi.org/10.5194/amt-11-5701-2018

Yuan, T., Remer, L.A., Pickering, K.E., & Yu, H. (2011). Observational evidence of aerosol enhancement of lightning activity and convective invigoration. *Geophys. Res. Lett*., 38, L04701. https://doi.org/10.1029/2010GL046052

Zhu, Y., Yu, X., Li, Z., & Rosenfeld, D. (2015). Separating aerosol microphysical effects and satellite measurement artifacts of the relationships between warm rain onset height and aerosol optical depth. *J. Geophys. Res. Atmos.*, 120. https://doi.org/10.1002/2015JD023547

Zipser, E. J., & Lutz, K.R. (1994). The Vertical Profile of Radar Reflectivity of Convective Cells: A Strong Indicator of Storm Intensity and Lightning Probability? *Mon. Wea. Rev.*, 122, 1751–1759. doi: 10.1175/1520-0493(1994)122<1751:TVPORR>2.0.CO;2

Zipser, E.J., Cecil, D.J., Liu, C., Nesbitt, S.W., & Yorty, D.P. (2006). Where are the most intense thunderstorms on Earth? *Bulletin of the American Meteorological Society*, *87*(8), 1057-107